

RSC Advances



This is an *Accepted Manuscript*, which has been through the Royal Society of Chemistry peer review process and has been accepted for publication.

Accepted Manuscripts are published online shortly after acceptance, before technical editing, formatting and proof reading. Using this free service, authors can make their results available to the community, in citable form, before we publish the edited article. This *Accepted Manuscript* will be replaced by the edited, formatted and paginated article as soon as this is available.

You can find more information about *Accepted Manuscripts* in the [Information for Authors](#).

Please note that technical editing may introduce minor changes to the text and/or graphics, which may alter content. The journal's standard [Terms & Conditions](#) and the [Ethical guidelines](#) still apply. In no event shall the Royal Society of Chemistry be held responsible for any errors or omissions in this *Accepted Manuscript* or any consequences arising from the use of any information it contains.



Journal Name

ARTICLE

Zn(II) complex with 2-quinolinecarboxaldehyde selenosemicarbazone: synthesis, structure, interaction studies with DNA/HSA, molecular docking and caspase-8 and -9 independent apoptosis induction†

Received 00th January 20xx,
Accepted 00th January 20xx

DOI: 10.1039/x0xx00000x

www.rsc.org/

Nenad R. Filipović^a, Snežana Bjelogrić^b, Aleksandar Marinković^c, Tatjana Ž. Verbić^d, Ilija N. Cvijetić^e, Milan Senčanski^f, Marko Rodić^g, Miroslava Vujčić^h, Dušan Sladić^d, Zlatko Striković^d, Tamara R. Todorović^{*d}, Christian D. Müller^{*i,j}

New Zn(II)-based potential chemotherapeutic agent was synthesized from the ligand 2-quinolinecarboxaldehyde selenosemicarbazone (Hqasesc). Single crystal X-ray diffraction analysis showed that Zn(II) complex consists of cation $[Zn(Hqasesc)_2]^{2+}$, two perchlorate anions and one ethanol solvent molecule. The interaction of calf thymus (CT) DNA and human serum albumin (HSA) with Zn(II) complex was explored using absorption and emission spectral methods, and also has been supported by molecular docking studies. The complex has more affinity to minor DNA groove than major, with no significant intercalation. The HSA interaction studies of the complex revealed the quenching of intrinsic fluorescence of the HSA through a static quenching mechanism. The antitumor activity of the ligand and the complex against pancreatic adenocarcinoma cell line (AsPC-1) and acute monocytic leukemia (THP-1) cells was evaluated. Both compounds are strong concentration-dependent apoptosis inducers in THP-1 cells. While Hqasesc in AsPC-1 cells induces apoptosis only at the highest concentration, treatment with Zn complex shows concentration-dependent apoptotic response, where treated cells are arrested in the G1-to-S phase accompanied with extensive activation of caspase-8 and -9. These results indicate that the ligand and Zn(II) complex display cell phenotype specific activity.

Introduction

Thiosemicarbazones are condensation products of thiosemicarbazide and carbonyl compounds, which have been extensively studied as NS bidentate ligands in coordination chemistry. They possess imine nitrogen and sulfur donor atoms from thiosemicarbazide moiety.^{1,2} Coordination capacity of this class of ligands may be extended if there is donor atom(s) from carbonyl compound in position(s) suitable to form chelate ring(s). This class of compounds is well known to possess a wide range of pharmacological properties.³ Studies from 1960s indicated that mechanism of action of thiosemicarbazones involves the inhibition of DNA synthesis.⁴ When it was proven that tumor cells lose their ability to convert ribonucleotides to deoxyribonucleotides after treatment with *N*-heteroaromatic thiosemicarbazone obtained from 2-formylpyridine, ribonucleotide reductase (RR) was marked as the main target for NNS chelating thiosemicarbazones. Chelation of iron from RR active site was proposed to be the reason for enzyme inactivation.⁴ The recent findings indicate other mechanisms of thiosemicarbazones action: reactive oxygen species (ROS) generation, DNA binding, topoisomerase II inhibition, mitochondria disruption, inhibition of protein synthesis and multidrug resistance protein inhibition.⁴⁻⁶

^a Faculty of Agriculture, University of Belgrade, Nemanjina 6, Belgrade, Serbia.

^b National Cancer Research Center of Serbia, Pasterova 14, Belgrade, Serbia.

^c Faculty of Technology and Metallurgy, University of Belgrade, Karnegijeva 4, Belgrade, Serbia.

^d Faculty of Chemistry, University of Belgrade, Studentski trg 12-16, Belgrade, Serbia; E-mail: tamarat@chem.bg.ac.rs

^e Innovation Center of the Faculty of Chemistry, University of Belgrade, Studentski trg 12-16, Belgrade, Serbia.

^f Center for Multidisciplinary Research, Institute of Nuclear Sciences "Vinča", University of Belgrade, Belgrade, Serbia.

^g Department of Chemistry, Faculty of Sciences, University of Novi Sad, Trg Dositeja Obradovića 4, Novi Sad, Serbia.

^h Institute of Chemistry, Technology and Metallurgy, University of Belgrade, Njegoševa 12, Belgrade, Serbia.

ⁱ Laboratoire d'Innovation Thérapeutique, UMR 7200, Faculté de Pharmacie, Université de Strasbourg, 67401 Illkirch, France.

^j Plateforme eBioCyt, Faculté de Pharmacie & Fédération Translationnelle de Médecine, Université de Strasbourg, 67401 Illkirch, France; E-mail: cdmuller@unistra.fr

† Electronic Supplementary Information (ESI) available: FT-IR (Fig. S1) and NMR (Figs. S2-S9) spectra; cyclic voltammograms (Fig. S10); pH dependent UV-Vis spectra (Figs. 11 and 12); packing diagrams (Fig. S13 and S14); sigmoidal dose-response curves (Fig. S15); Stern-Volmer plot (Fig. S16); modified Stern-Volmer plot (Fig. S17); the plot of $\ln K_b$ vs. $1/T$ (Fig. S18); double-log plot (Fig. S19); fluorescence spectral overlap (Fig. S20); conformations of the complex in the DNA duplex (Fig. S21); the location of HSA-Zn complex binding site (Fig. S22); Numbering of atoms (Scheme S1); hydrogen bonding geometry (Table S1); interactions of HSA binding site (Table S2). CCDC 1413656 and 1413657. For ESI and crystallographic data in CIF or other electronic format see DOI: 10.1039/x0xx00000x

Despite the fact that various thiosemicarbazones have been developed and even patented as pharmaceuticals,⁷ synthesis and biological activity investigation of this type of compounds is still the topic of interest. Some recent studies resulted in new thiosemicarbazone molecules, which are more active than standard chemotherapeutics.^{8–13} One strategy for improvement of biological activity of thiosemicarbazones is synthesis of their metal complexes. Coordination of thiosemicarbazones to metals enhances their lipophilicity by orienting lipophilic and aromatic parts outwards the complex molecules toward the solvent.⁶ Metal complexes may be a vehicle for the activation of thiosemicarbazones by increasing their ability to diffuse through the semipermeable membrane of cells, and complexes often show less side effects and different bioactivities in comparison to metal-free ligands.³

Selenosemicarbazones are selenium analogues of thiosemicarbazones and their biological activity has been studied in less extent, probably because selenium was considered as a toxic element for humans up to late fifties.¹⁴ Another reason might be the instability of this type of compounds as is apparent from the precipitation of elemental selenium during the complexation of selenosemicarbazones, modification of ligands with evolution of hydrogen selenide, or oxidation with the formation of diselenide bridges.¹⁴ However, some of synthesized selenosemicarbazones and their complexes showed good biological activity.^{15–18} Few comparative studies indicated that selenosemicarbazones showed similar or even better biological activities than corresponding thiosemicarbazones and their complexes.^{19–24} We previously synthesized and characterized Zn(II) complexes with *N*-heteroaromatic selenosemicarbazones of 2,6-diacetylpyridine, 2-formylpyridine and quinoline-2-carboxaldehyde (H₂dapsesc, Hfapsesec and Hqasesc, respectively).^{25–27} In corresponding complexes the ligands were coordinated *via* N_{aromatic}, N_{imin}, and Se atoms. The Zn complexes with pyridine derivatives were subject of antitumor investigations,^{27–31} while complex with quinoline derivative was unsuitable due to low solubility. The complex with H₂dapsesc showed a strong dose-dependent cytotoxic activity, with IC₅₀ value in the range 13–60 μM on six human carcinoma cell lines, as determined by colorimetric assay after 24 h incubation.³⁰ On human breast cancer (MDA-361) and human colon cancer (LS174) cell lines, the IC₅₀ values for this complex were of the same order of magnitude as IC₅₀ values of cisplatin (CDDP). The Zn complex with formylpyridine derivative showed strong cytotoxic effect on five treated human cancer cell lines, in the range of the activity of CDDP, as determined by colorimetric assay after 48 and 72 h of incubation.²⁷ It is worth mentioning that this complex had a low toxicity on normal endothelial cells (EA.hy926), lower in comparison to the activity on treated cancer cell lines, and even lower than the activity of CDDP on EA.hy926 cells.

In order to continue our investigation on antitumor activity of selenosemicarbazone complexes with biometals we have synthesized a new Zn complex with Hqasesc ligand and evaluated ligand and complex activities on a different cancer cell model than used in our previous studies. While organizing

current research, our guiding idea was to test whether these compounds can display full-scale anticancer activity. Extensive research of cancer biology and behavior has revealed that the same cells, which mediate tumor growth, are also responsible for resistance to treatment and tumor relapse, and those have been referred as Cancer Stem Cells (CSCs).³² Important feature of CSCs is their extensive genomic heterogeneity, which results in persistent cancer sub-clones with a unique genomic and epigenomic profile, and each of those sub-clones are probably endowed with different drug-resistant phenotype. Furthermore, it was shown that another characteristic of CSCs is the reversible transition between epithelial and mesenchymal states in carcinoma. Epithelial-mesenchymal transition (EMT) is a physiological process that occurs during embryonic development, which is defined by biochemical changes in epithelial cells that lead to the acquisition of mesenchymal properties, including loss of cell adhesion and increased migratory capacity.³³ In cancer, EMT generates cells with apparent CSC features and has been associated with more aggressive tumors.³⁴ Therefore, evidences from experimental models and clinical studies strongly indicate that the major goal of the current drug development is to create efficient strategic drug with ability to induce apoptotic death in all tumor cells including CSCs, as the only way to achieve cancer cure. For that reason, in the present work we have explored the activity of Hqasesc ligand and its Zn complex against pancreatic adenocarcinoma cell line (AsPC-1), which possesses characteristics of epithelial-mesenchymal transition (EMT)-type cells, bearing resistance to three conventional chemotherapeutic agents (gemcitabine, 5-fluorouracil, and CDDP).^{35,36} Antitumor activity of the compounds was also evaluated on non-CSC acute monocytic leukemia (THP-1) cells. Owing to noted characteristics, the chosen cell lines represent excellent *in vitro* models for the investigation of Hqasesc ligand and its Zn complex against heterogeneity and plasticity of cancer cells.

Results and discussion

Zn(II)-complex with the ligand Hqasesc was prepared by template reaction starting from zinc(II) perchlorate hexahydrate, 2-quinolinecarboxaldehyde and selenosemicarbazide (mole ratio 1 : 2 : 2, respectively). The complex is soluble in MeOH, EtOH, MeCN, DMF and DMSO at room temperature. Molar conductivity measurements showed that the complex is 1 : 2 electrolyte. Based on these results, as well as results of elemental analysis, spectroscopic and X-ray diffraction study (*vide infra*), the formula of the complex can be written as [Zn(Hqasesc)₂](ClO₄)₂·EtOH (1).

IR and NMR spectroscopy

Experimental IR spectrum of **1** (Fig. S1a, ESI) was interpreted in terms of a calculated one (Fig. S1b, ESI) at B97D/TZVP level of theory (see experimental section for details) and with comparison to the spectrum of metal-free ligand. In the IR spectrum of Hqasesc there are sharp medium intensity bands

in the region 3340 – 3080 cm^{-1} which are assigned to the $\nu(\text{NH}_2)$ and $\nu(\text{NH})$ stretching vibrations.²⁶ The lack of large systematic shift of these bands in the IR spectrum of **1** indicates no interaction between the terminal nitrogen atom and zinc ion. As it had been previously observed in other selenosemicarbazone complexes,^{25–28} in the IR spectrum of **1** there is a systematic shift of the $\nu(\text{C}=\text{N})$ band to higher frequency in comparison to that in the corresponding ligand (1607 cm^{-1} in Hqasesc; 1617 cm^{-1} in **1**). Also, in the spectrum of **1** the sharp and strong band at $\sim 1100 \text{ cm}^{-1}$ originating from perchlorate ion can be observed.

1D (^1H and ^{13}C) and 2D (COSY, NOESY, ^1H – ^{13}C HSQC and ^1H – ^{13}C HMBC) spectra of **1** were recorded in DMSO- d_6 and are shown in Figs. S2–S7 (ESI) together with an atom numbering scheme (Scheme S1, ESI). NMR spectral data for Hqasesc are in full agreement with previously published data.²⁶ In all 1D spectra of **1** there is only one set of signals, indicating the presence of just one form of the complex in the solution. Based on the presence of the H–N3 signal at 12.56 ppm in ^1H NMR spectrum of **1**, the ligand is coordinated to Zn(II) in the neutral form. It has already been documented that NMR signal shifts for Zn-thio(seleno)semicarbazone complexes in comparison to corresponding signals for free ligands are less pronounced than for other chalcogensemicarbazone d -metal complexes.^{25,27,37,38} Coordination of Zn(II) ion to Hqasesc gives rise to downfield shifts of all protons in ^1H NMR spectrum (Fig. S8a, ESI), together with shifts of almost all signals in ^{13}C NMR spectrum (Fig. S8b, ESI). The quinoline nitrogen atom coordination is corroborated by significant downfield shift of signal of C4–H in proton NMR and signal of C4 in carbon NMR spectrum, as well as upfield shift of signals of C8a and C2 in carbon NMR spectrum of **1**. Downfield shift of C9 signal in ^{13}C NMR spectrum indicates imine nitrogen coordination, while due to selenium atom coordination the signals of N4Ha and N4Hb are significantly shifted downfield. A shift of the signal of selenone carbon atom (C=Se) in the spectrum of **1** is similar to those reported for analogous Zn-chalcogenesemicarbazone complexes.^{25,27,37} The complex **1** was quite stable, as can be seen from the proton spectra of freshly prepared sample and sample after 24 h (Fig. S9, ESI).

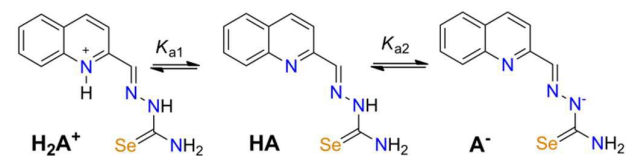
Cyclic voltammetry

The redox behavior of Hqasesc and **1** have been investigated by cyclic voltammetry (Fig. S10, ESI) in the potential range from +1.2 to –2.0 V relative to a Ag/AgCl reference electrode. Repeated scans, as well as different scan rates, showed that dissociation of the ligand does not take place in **1**. In the cyclic voltammogram of the ligand, two cathodic peaks at –1.38 and –1.93 V vs Ag/AgCl were observed. The first peak can be attributed to imine bond reduction since similar value (–1.33 V) was assigned to a pyridinium analogue of Hqasesc.³⁹ It is reasonable to assume that second peak resulted from selenamide reduction. Namely, similar values for benzil, bis(thiosemicarbazone) (–1.440 and –1.746 V vs Ag/AgCl) were assigned to imine and thioamide reduction, respectively.⁴⁰ In the reverse scan process, no anodic peaks were

observed, indicating that these electrochemical processes were coupled with a chemical reaction (EC mechanism).⁴¹ In the cyclic voltammogram of **1** the corresponding cathodic peaks are shifted to the positive positions (–1.35 and –1.84 V vs Ag/AgCl) due to the metal–ligand orbital interactions, as it was noticed for Zn complex with 4-phenyl-1-[(4-methoxyphenyl)methylene]thiosemicarbazide.⁴² In the range from 0 to –1.3 V additional reduction peaks are observed in the cyclic voltammogram of **1**, as in the case of Zn–benzil, bis(thiosemicarbazone) complex.⁴⁰ The number of reduction peaks is equal for Hqasesc and **1** which indicates that the complex is stable - Zn(II) ion is “hidden” for reduction in the chelate structure. On the other hand, the number of oxidation peaks in the cyclic voltammograms of Hqasesc and **1** is different (Hqasesc: 0.32 and –0.02 V vs Ag/AgCl; **1**: 0.30, –0.04 and –0.52 V vs Ag/AgCl). Additional oxidation peak can be assigned to Zn(II) ion oxidation, which is proven by addition of $\text{Zn}(\text{ClO}_4)_2 \times 6\text{H}_2\text{O}$ in a solution of **1** (Fig. S10, ESI).

Determination of acidity constants of Hqasesc

Acidity constants of the ligand were determined using spectrophotometric titration at $T = 298 \pm 1 \text{ K}$. Within studied pH range (1.65–11.91) Hqasesc acts as sparingly soluble ampholyte (Scheme 1).



Scheme 1. Protolytic equilibria of Hqasesc in aqueous media. HA, as neutral form of Hqasesc, is represented with one tautomeric form, while all tautomers coexist in solution.

UV-Vis spectra of Hqasesc in pH ranges 1.65–5.17 and 5.17–11.91 are shown in Figs. S11a and S12a (ESI). The existence of two pH regions with clearly visible isobestic points indicates that two pK_a values are well separated ($\Delta\text{pK}_a > 3$). Existence of isobestic points proves that the only process in the solution within both pH ranges is a protolytic equilibrium shown in Scheme 1. This makes spectrophotometric method valid for pK_a values determination. Acidity constant (K_{a1} and K_{a2}) values were calculated according to transformed forms of classical spectrophotometric equation,⁴³ which gives linear dependence (for details see experimental part). A value of K_{a1} was obtained as a slope from corresponding linear dependences at four wavelengths (287, 327, 341, 390 nm), while K_{a2} was obtained as a slope from corresponding linear dependences at three wavelengths (266, 330, 365 nm). Examples are shown in Figs. S11b and S12b (ESI). Obtained pK_{a1} and pK_{a2} values are given in Table 1 and the corresponding distribution diagram in Fig. 1. It should be noted that all determined constants represent macro ionization constants. As shown in Scheme 1, K_{a1} represent the dissociation of protonated quinoline nitrogen, while K_{a2} accounts for different contributions of

Se1–Zn1–N2–N3–C1, which is significantly puckered, and may be described as twisted on Zn1–N2 bond. Coordination octahedron is distorted, as a consequence of constraints implied by ligand's bite angles which are in the range 73.74(7)–79.44(5)°.

Table 3. Selected bond lengths (Å) and bond angles (°) of Hqasesc and **1**.

	Hqasesc	1
Zn1–Se1	—	2.6233(3)
Zn1–Se1A	—	2.5592(3)
Zn1–N1	—	2.2211(17)
Zn1–N1A	—	2.2177(17)
Zn1–N2	—	2.1971(18)
Zn1–N2A	—	2.1808(18)
C2–N2	1.278(3)	1.275(3)
C2A–N2A	—	1.271(3)
N2–N3	1.364(3)	1.355(3)
N2A–N3A	—	1.362(3)
C1–N3	1.348(3)	1.339(3)
C1A–N3A	—	1.340(3)
C1–Se1	1.841(2)	1.842(3)
C1A–Se1A	—	1.842(2)
N1–Zn1–N2	—	73.74(7)
N1A–Zn1–N2A	—	74.02(7)
N2–Zn1–Se1	—	77.84(5)
N2A–Zn1–Se1A	—	79.44(5)
N1–Zn1–Se1	—	149.70(5)
N1A–Zn1–Se1A	—	152.98(5)

Metal–ligand bonds fall in wide range (2.1808(18)–2.6233(3) Å), which is in line with different covalent radii of nitrogen and selenium donor atoms. Quinoline nitrogen atoms form slightly longer bonds than azomethine nitrogen atoms, which is also observed in Ni(II) and Co(III) complexes with Hqasesc.^{26,46} On the other hand, significantly longer bonds are formed between Se and Zn atoms, as expected. It is worth mentioning that Zn–Se bonds are not equivalent, and that Se1 atom forms almost 0.1 Å longer bond [2.6233(3) Å] compared to Se1A [2.5592(3) Å]. Moreover, Se1 atom is part of the only significantly puckered metallocycle. Ligand deformation occurs in a way that distance between Se1 and Se1A is maximized (Se1...Se1A = 3.8831(3) Å). This can be visualized by torsion angles $\tau(\text{C2–N2–N3–C1}) = -169.7(2)^\circ$, and $\tau(\text{N2–N3–C1–Se1}) = -6.9(3)^\circ$. Similar behavior is observed in $[\text{Ni}(\text{qasesc})_2]$, where Se...Se distance is 3.7955(5) Å however, in that complex, both ligands are equally deformed, whereas in $[\text{Zn}(\text{Hqasesc})_2]^{2+}$ only one ligand is deformed. The proposed plausible explanation says that bis-ligand structure of the cation places two selenium atoms closer than the sum of their van der Waals (VdW) radii ($r_{\text{Se}} = 1.9$ Å), and distortion is the consequence of steric repulsion.²⁶ Nevertheless, in $[\text{Co}(\text{qasesc})_2]\text{BF}_4 \cdot 2\text{H}_2\text{O}$ and Fe(III) complex $[\text{Fe}(\text{L})_2][\text{FeCl}_4] \cdot 1/3\text{MeCN}$ (HL = 3-azabicyclo[3.2.2]nonane-3-carboselenoic acid, [1-(2-pyridinyl)ethylidene]hydrazide)⁵⁰ the Se...Se distances [3.349(1) and 3.494(3) Å, respectively] are significantly less than the sum of their VdW radii. The comparison of M–Se bond lengths and Se...Se distances in above mentioned

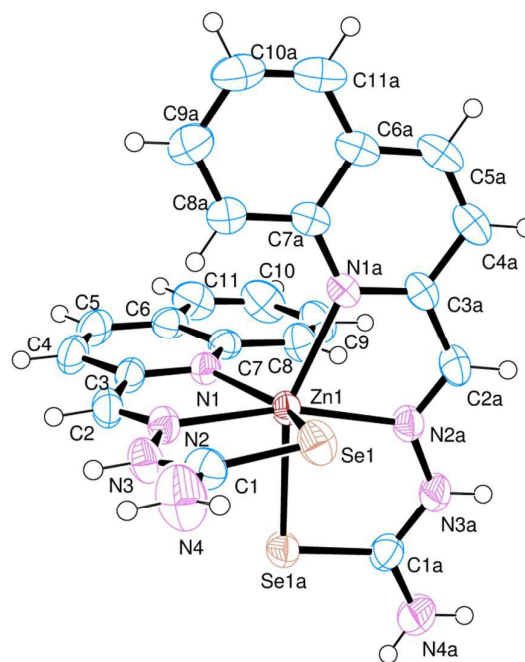


Fig. 3 The ORTEP diagram of complex cation $[\text{Zn}(\text{Hqasesc})_2]^{2+}$ in **1** drawn at 50% probability level.

shows that these properties are approximately in direct proportion. Since Se...Se distances in Co(III) and Fe(III) complexes are shorter than a sum of VdW radii, it appears that in those cases the strength of the coordination bonds compensate steric repulsion, whereas in Ni(II) and Zn(II) complexes the longer metal–ligand bonds allow deformation of the coordination polyhedron to minimize steric repulsion between non-bonded adjacent Se atoms.

Intra-ligand bond lengths in the structure of **1** are quite similar to those found in free ligand. The CSD search for C–Se single and double bond length distribution in Se-coordinated compounds having N–C(–Se)–N fragment, reveals very broad and overlapped ranges: 1.81–1.93 Å (67 hits, mean = 1.87(2) Å) for formal double bonds, and 1.81–1.97 Å (58 hits, mean = 1.88(3) Å) for formal single bonds. In this context, Se1–C1 and Se1A–C1A bond lengths in the complex (1.842(3) and 1.842(2) Å, respectively) are slightly shorter than the average C=Se double bond in compounds with structurally related fragments.

Overall crystal structure is comprised of interleaved cation sheets and anion + solvent sheets, progressing parallel to the *ac* plane (Fig. S14, ESI). In addition to the electrostatic attraction, cations and perchlorate anions are connected with numerous hydrogen bonds. The two selenosemicarbazone moieties of a cation are differently involved in those interactions as hydrogen bond donors. Namely, N(4)H₂ and N(3)H groups are bonded exclusively to perchlorate oxygen atoms, whereas N(4A)H₂ and N(3A)H groups are bonded to ethanol oxygen, while N(4A)H₂ group is additionally bonded to another perchlorate anion. The only significant cation–cation interaction within the sheet is the weak N4A–H4D...Se1ⁱⁱⁱ (*iii*:

$-x, y -1/2$) hydrogen bond (Table S1, ESI). The hydroxyl group of ethanol molecule exhibits positional disorder, and in both sites (O9A and O9B) it acts as N(3A)H hydrogen bond acceptor, but acts as hydrogen bond donor to perchlorate anions in opposite directions.

Free radical-scavenging activity

Because selenium antioxidants can prevent oxidative damage, numerous animal and clinical trials have investigated the ability of these compounds to prevent the oxidative stress that is an underlying cause of cancer. Interest in selenoneine, a compound which effectively scavenges 1,1-diphenyl-2-picrylhydrazyl (DPPH) radical.⁵¹ In our previous study free radical-scavenging activity of selenosemicarbazones and their metal complexes by ABTS [(2,2'-azino-3-bis(ethylbenzthiazoline-6-sulfonic acid) radical cation) method were determined.¹⁴ Our results showed that Hqasesc and its isomeric analogue H8qasesc (8-quinolinecarboxaldehyde selenosemicarbazone) had an excellent ABTS cation radical-scavenging effect, which was greater than that of reference antioxidant vitamin C. Coordination to Pt(II), Pd(II), Cd(II), Co(III) and Ni(II) reduced the antioxidant activity in corresponding complexes. However, some selenosemicarbazone complexes still showed better activity than vitamin C.¹⁴

The proton donating ability of the Hqasesc and **1** was assayed using protocol for determination of radical scavenging activity, the DPPH method.⁵² IC₅₀ values were calculated from the plotted graph of scavenging activity against the concentrations of the samples. IC₅₀ is defined as the total antioxidant necessary to decrease the initial DPPH radical by 50%. IC₅₀ was calculated for all compounds based on the percentage of DPPH radicals scavenged. Ascorbic acid was used as the reference compound (positive control) with concentrations from 50 to 500 µg/mL. These results corroborate our previous finding obtained with ABTS method that Hqasesc has excellent free radical-scavenging activity, better than vitamin C. Coordination to Zn reduces the activity of corresponding complex **1**, but still **1** is two times more active than vitamin C.

Evaluation of pro-apoptotic activity

Initial experiment was organized to test ability of Hqasesc and **1** to induce cell death in treated malignant populations. Both compounds were applied in a range of six concentrations and left for 24 h on THP-1 and AsPC-1 cells. Afterwards, cells were evaluated for occurrence of cell death in terms of quality and quantity. There are several modalities of cell death that are classified according to morphological characteristics and measurable biochemical features.⁵³ In the current study Annexin-V/propidium iodide (PI) staining was used, *i.e.* a quantitative method that provides objective assessment of cell viability alongside with accurate incidence of apoptotic and necrotic cells in analyzed sample. This method is based on detection of phosphatidylserine (PS) externalization in the

plasma membrane surface of apoptotic cells. This is the earliest event in this programmed cell death arisen as one of the "eat-me" signals that contributes to the recognition and removal of apoptotic bodies by phagocytosis.⁵⁴ The PS is also a binding site for Annexin-V, while PI serves as a cell membrane non-permeant dye excluded from viable cells. Such double assay staining allows differentiation between viable cells and those in apoptosis: early (Annexin-V positive cells), late stages (Annexin-V and PI positive cells) and necrosis (PI only stained cells).

As represented in Fig. 4, both compounds on THP-1 cells induced concentration-dependent increase in percentage of apoptotic cells, while appearance of necrosis was at the level of untreated control. In cells treated with Hqasesc, apoptosis was detected starting from concentration of 30 µM, which also was the concentration that induced the highest percent of double-stained cells. The increase of Hqasesc concentration on treated cells was followed by rise of early apoptotic events and sequential reduction of cells in late apoptosis, whereas percentages of vital cells were remaining almost the same in samples treated within the range 30–75 µM. Treatment with **1** induced massive apoptosis already at concentration of 10 µM. It is interesting that at this concentration almost all apoptotic cells were in the late stages whereas incidence of pre-apoptotic events was barely above non-treated control. As concentration of **1** was ascending, percentage of early apoptotic cells was increasing at the expense of viable cells while the incidence of double stained cells remained unchanged. Contrary to Hqasesc and **1**, treatment of THP-1 cells with CDDP induced only their accumulation at the early phase of apoptosis. Even the escalation of CDDP concentration could not facilitate execution and termination of apoptosis after 24 h of incubation. It is expected from a successful anticancer agent not only to trigger apoptotic death, but also to conduct the cells through the whole process of programmed cell death. If all chains of cascaded actions of apoptosis are accomplished within a short period of time, the treated cell will have less chance to develop resistance to the mechanism which initiated apoptotic response. Therefore, compared to CDDP both Hqasesc and **1** displayed more favorable mode of activity on THP-1 cell line.

Likewise, a striking lack of early apoptotic events was also evident in AsPC-1 cells treated with **1** (Fig. 5). In these cells first double-stained events were readout in samples treated with **1** at 30 µM, and their percentage was increasing dependently on concentration of **1**. On the other hand, in AsPC-1 cells treated with Hqasesc, apoptosis was found only in sample treated with the highest applied concentration and was not accompanied by an increasing percentage of necrotic cells. These results left unclear whether THP-1 and AsPC-1 cells, labeled with both Annexin-V and PI, after treatment with **1** were actually apoptotic or necrotic since it was shown that double-stained cells can be interpreted as both.⁵⁵ In order to make a clear discrimination between apoptosis and necrosis as the endpoint event of the treatments, we decided to manipulate these two possible scenarios by using shorter incubation periods with a single appointed concentration of each

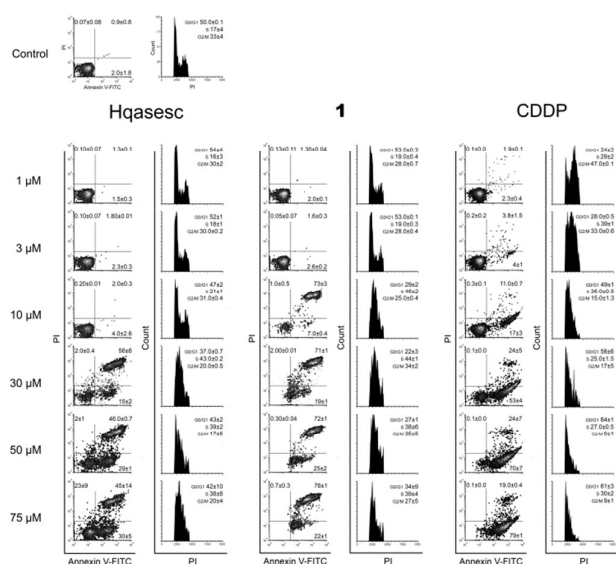


Fig. 4 Activity of Hqasesc, **1** and CDDP on THP-1 cells. Annexin-V and PI double staining (left panels for apoptosis) and PI single staining (right panels for cell cycle) of THP-1 cells after 24 h treatment with Hqasesc, **1** and CDDP applied in a range of six dose concentrations. In Annexin-V/PI plots cells are discriminated as viable (non-stained cells, lower left quadrant), cells in early phases of apoptosis (Annexin-V single stained cells, lower right quadrant), cells in late phases of apoptosis (double-stained cells, upper right quadrant), and cells in necrosis (PI single stained cells, upper left quadrant). The same cells evaluated with Annexin-V/PI were fixed in ethanol right after analysis, left overnight and assayed the next day for cell cycle phases of mitotic division with PI single staining method after RNase treatment. Frequency of cells found in G0/G1, S and G2/M phases was determined according to non-treated control population. All results are expressed as the mean \pm SD of two replicates from independent experiments, while compounds were placed on the same microtiter plate in both experiments with the same non-treated control for Annexin-V/PI and cell cycle analysis.

compound. This concentration was chosen to be the ED₅₀ computed according to percentage of Annexin-V labeled cells irrespectively of PI positive cells. As seen from dose-response curves (Fig. S15, ESI), both Hqasesc and **1** showed significantly stronger activities against THP-1 cells, with several times higher ED₅₀ concentrations on AsPC-1 cell line. The ED₅₀ concentration for CDDP on THP-1 cells was comparable to the value for Hqasesc, but three times higher compared to **1**. On AsPC-1 cell line CDDP did not induce neither significant percentage of cell death, nor ED₅₀ changes.

Impact on apoptotic responses of co-incubation with the pancaspase inhibitor Z-VAD-fmk

Apoptosis is a process of biochemical events that lead to characteristic morphological changes of the cell and finally its death. These biochemical events are predetermined and include cascaded activations of different effectors, starting from a triggering incidence up to mitochondrial outer membrane permeabilization, which is marked as the “point of no return” of the lethal process.⁵³ The central role in regulation of apoptosis belongs to caspases, a family of cysteine proteases. If caspases play an essential role in THP-1- and AsPC-1-treated cells, then the pancaspase inhibitor *N*-benzyloxycarbonyl-Val-Ala-Asp(O-Me) fluoromethyl ketone

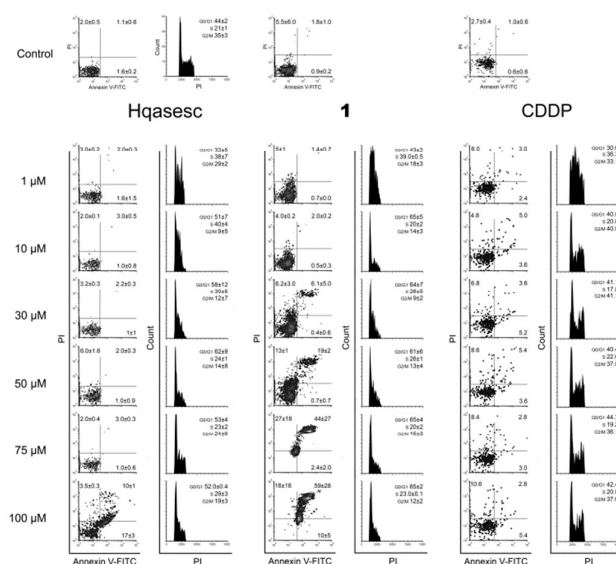


Fig. 5 Activity of Hqasesc, **1** and CDDP on AsPC-1 cells. Annexin-V and PI double staining (left panels for apoptosis) and PI single staining (right panels for cell cycle) of AsPC-1 cells after 24 h treatment with Hqasesc, **1** and CDDP applied in a range of six dose concentrations. In Annexin-V/PI plots, cells are discriminated as viable (non-stained cells, lower left quadrant), cells in early phases of apoptosis (Annexin-V single stained cells, lower right quadrant), cells in late phases of apoptosis (double-stained cells, upper right quadrant), and cells in necrosis (PI single stained cells, upper left quadrant). The same cells evaluated with Annexin-V/PI were fixed in ethanol right after analysis, left overnight and assayed the next day for distribution within phases of mitotic division with PI single staining method in presence of RNase. Frequency of cells found in G0/G1, S and G2/M phases was determined according to non-treated control population. All results for Hqasesc and **1** are expressed as the mean \pm SD of two replicates from independent experiments. Results for CDDP are expressed as the % of gated cells from one replicate considering the additional experiment was not performed due to inactivity of CDDP on AsPC-1 cells. Investigated compounds were placed on different plates, with separate non-treated control cells for Annexin-V/PI reading, while the control for cell cycle analysis represents the mean \pm SD of five replicates.

(Z-VAD-fmk) should inhibit treatment-dependent response. We performed a 6 h co-incubation of Z-VAD-fmk with either Hqasesc or **1** applied at their ED₅₀ concentrations on THP-1 and AsPC-1 cells, respectively, while effect of Z-VAD-fmk on apoptosis induced by CDDP was investigated only on THP-1 cell line. After incubations, cells were stained with Annexin-V/PI, and percentages of cell death inhibition were computed taking all Annexin-V positive events into account (Fig. 6A).

According to the percent of inhibited apoptotic response for Z-VAD-fmk co-treated cells, all investigated compounds induced apoptosis by both, caspase-dependent and caspase-independent pathways. In THP-1 cells, average reduction of apoptotic death varied from 20 to 35% with no significant difference between treatments. On the contrary, the addition of Z-VAD-fmk to Hqasesc and **1** treatment on AsPC-1 cells had higher impact on cell survival as compared to THP-1 cells. These results indicated that Hqasesc and **1** induce apoptosis in THP-1 and AsPC-1 cell line by different pathways. Also, the high percent of apoptosis reduction by Z-VAD-fmk in AsPC-1 cell line treated with **1** clearly indicates that double-stained

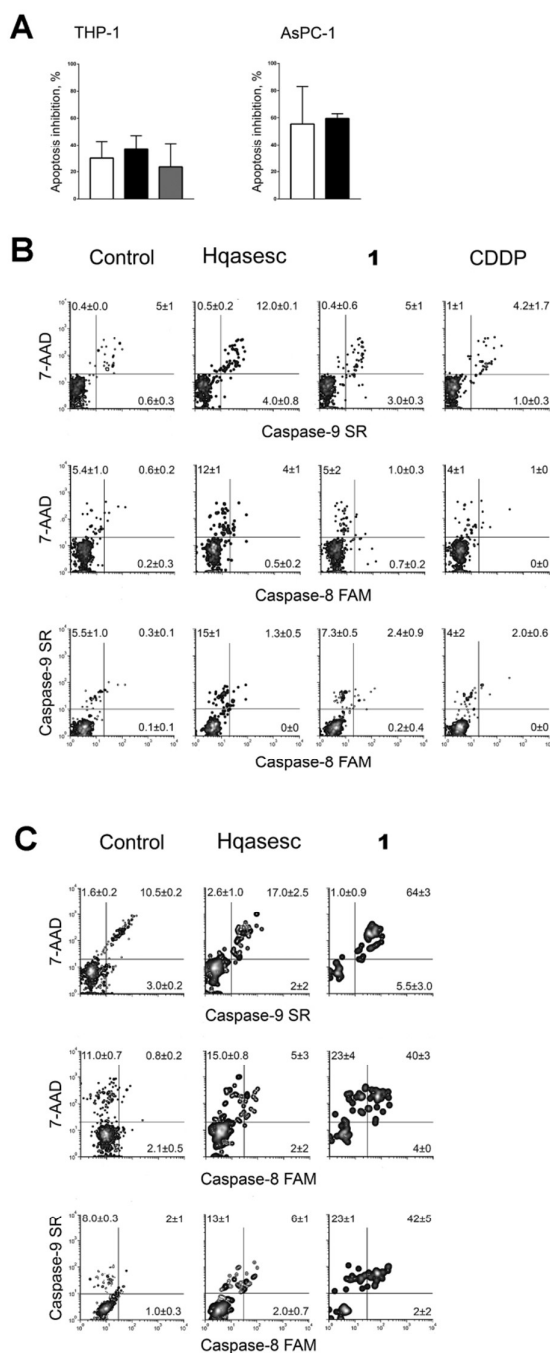


Fig. 6 (A) Percent of apoptosis inhibition induced by 6 h co-incubation of Hqasesc (white bar), **1** (black bar) and CDDP (gray bar) applied in ED_{50} concentrations with pancaspase inhibitor Z-VAD-fmk. Results are expressed as the mean \pm SD of two replicates from independent experiments. Role of caspases in apoptosis induced by Hqasesc, **1** and CDDP. Caspase-8 and -9 activities determined in cells after 6 h incubation with Hqasesc, **1** and CDDP on THP-1 cells (B) and Hqasesc and **1** on AsPC-1 cells (C), all applied in ED_{50} concentrations. In the plots cells are discriminated as live (not stained with either caspase nor 7-AAD), mid stage apoptotic cells (cells stained with either caspase-8 or -9, but negative to 7-AAD), late stage apoptotic cells (cells stained with either of caspase-8 or -9 and with 7-AAD), and necrotic cells (cells not stained with either caspase-8 nor -9, but positive for 7-AAD). Results are expressed as the mean \pm SD of two replicates from independent experiments.

events found after 24 h of incubation were cells in advanced phases of apoptosis rather than necrosis.

Assessment of caspase activity

Results with Z-VAD-fmk imposed the need to assess which pathway is activated in regulation of apoptotic death by treatment of the cells with Hqasesc and **1**. Caspases that regulate apoptosis can be divided in two major groups: caspase initiators (caspases 2, 8, 9, and 10), and caspase effectors (caspases 3, 6, and 7). Further, apoptosis can be triggered through different biochemical routes, which in general are divided in "intrinsic" and "extrinsic" pathways.^{56,57} Briefly, the term "extrinsic apoptotic pathway" indicates that apoptosis is triggered by extracellular death signals that are sensed and propagated by specific transmembrane receptors, a pathway regulated by caspase-8 or -10. Initiation of "intrinsic apoptotic pathway" comes as a result of bioenergetics and metabolic catastrophe triggering caspase-9. Therefore, we evaluated caspase-8 and -9 activities after 6 h of treatment at ED_{50} concentrations of Hqasesc and **1** in both cell lines.

Non-treated THP-1 cells show a constitutive caspase-9 activity, while activated caspase-8 was never recorded. After 6 h of treatment with Hqasesc, only a modest increase in caspase-9 activity was found whereas activity of caspase-8 stayed on the level of non treated cells (Fig. 6B). Incubation of THP-1 cells with **1** and CDDP did not induce increase in any activity of these two caspases. Such a result in the case of CDDP might be quite understandable considering it induced only a small percentage of cells in advanced phase of apoptosis, in correspondence to the percentage of apoptosis inhibited with Z-VAD-fmk co-treatment. However, as already discussed above, treatment of THP-1 cells with **1** induced a massive apoptotic response of low ED_{50} value with almost 40% of apoptosis inhibited by Z-VAD-fmk. All these facts indicate that there is probably another caspase-dependent pathway of apoptosis regulation involved other than caspase-8 and -9. For instance caspase-2 should be taken into consideration. A lack of known caspase-2 substrates has been the major obstacle for its categorization within one of the two major apoptotic pathways. Caspase-2 is activated by cellular stress induced by DNA damage, cytoskeletal disruption or radical oxygen species formation, and it acts in functional compensation with caspase-9.⁵⁸ Thus, further investigation will be required to identify the possible role of caspase-2 in THP-1 cell apoptosis induced by Hqasesc and **1**.

Constitutive activity of caspase-9 is also found in AsPC-1 cells. Again, incubation with Hqasesc resulted in a slight increase of caspase-9 and -8 activities (Fig. 6C). Quite the opposite, treatment with **1** triggered massive activation of both caspases. Such a result confirms that the complex **1** is a strong apoptotic inducer for AsPC-1 CSCs. Nevertheless, considerable impact of Z-VAD-fmk on apoptosis induced by Hqasesc indicates a possibility that its activity on AsPC-1 cells might also be related to the activation of caspase-2, rather than caspase-8 and -9.

Cell cycle distribution

In the current study certain improvements of the standard experimental protocols were applied. In particular, cells treated for 24 h and stained with Annexin-V/PI for evaluation of pro-apoptotic activity, after analysis on flow cytometer, were fixed overnight with ethanol and subsequently assessed for cell cycle distribution. This manipulation brought considerable advantages such as the decrease in amount of analyses, and more importantly the reduction of incidental divergences in experimental results since the same treated cells were used to provide two different but complementary readouts.

As represented in Fig. 4, Hqasesc and **1** stimulated THP-1 cells arrest in the S phase of mitotic division in a concentration-dependent manner. This phenomenon coincided with the occurrence of apoptosis. In AsPC-1 cells treatment with Hqasesc and **1** induced arrest at the S phase only at lowest concentration of 1 μM , which, following increase of applied concentrations, was shifted toward G1-to-S blockage (Fig. 5). Thus, the incidence of apoptosis in AsPC-1 cells could not be related to particular alteration in cell distribution within mitotic division. Interestingly, CDDP on THP-1 cells initially induced S-to-G2 arrest at the lowest applied concentration, shifting to a blockage in the S phase at 3 μM , and finally generated G1-to-S arrest, which matches with apoptotic response (Fig. 4). These results indicate the following: Hqasesc and **1** have different mode of activity on THP-1 compared to CDDP, and Hqasesc and **1** induce apoptosis in THP-1 and AsPC-1 cells by dissimilar mechanisms. One might suppose that Hqasesc and **1** in THP-1 cells interfere with DNA replication, while in AsPC-1 cells they initiate activation of G1/S checkpoints which impedes cell transition into S phase and the beginning of DNA replication. To determine the ability of more active compound (**1**) to interact with DNA, the next set of experiments on DNA binding and DNA cleavage were performed.

DNA binding studies

Non-covalent interactions of transition metal complexes with DNA include intercalation between the bases, binding to minor groove, major groove, sugar-phosphate backbone and three-way junction.⁵⁹ Electronic absorption spectroscopy is an effective method for examining the binding mode. The hypochromic effect induced by the DNA on a spectrum of a bound ligand is one indicator of the binding mode. In general, intercalators have stronger hypochromicities than the corresponding groove binders. The absorption spectra of metal complexes bound to DNA through intercalation exhibit significant hypochromism and red shift due to the strong $\pi \rightarrow \pi^*$ stacking interaction between the aromatic chromophore ligand of metal complex and the base pairs of DNA.⁶⁰ Metal complexes, which bind non-intercalatively or electrostatically with DNA, may result in either hyperchromism or hypochromism.⁶¹ Groove binding typically results in only subtle changes in the structure, and DNA remains essentially in an unperturbed B form. In contrast, intercalation in which a

planar ligand moiety is inserted between adjacent base pairs, results in a substantial change in DNA structure and causes lengthening, stiffening and unwinding of the helix. Zinc-containing compounds are regarded as one of the most promising alternatives to CDDP as anticancer drugs.⁶² It has been reported that zinc complexes can interact with DNA by different modes.^{63,64} In this work, spectroscopic methods were employed to ascertain the interaction mode of **1** with calf thymus (CT) DNA.

Electronic absorption spectra of **1** in aqueous buffer media, both in the absence and the presence of CT-DNA, are shown in Fig. 7. The absorption spectrum of **1** (Fig. 7A) exhibits two peaks (at 296 and 343 nm) and two shoulders (at 240–250 and 425–450 nm). The interaction of the complex with CT-DNA was monitored by disappearing of shoulder bands and peak at 296 nm. After interaction with CT-DNA, the absorption band at 343 nm exhibited hyperchromism of about -22% with the lowest concentration of **1**. With the increase of concentration of **1** (3×10^{-5} and 6×10^{-5} M), hypochromism (the value reaches 26% and 50%, respectively) followed by blue shift (10 nm at maximal performed concentration), occurs as the result of possible intercalative interactions between the complex and CT-DNA due to the strong stacking interaction between the aromatic chromophore of **1** and the base pairs of DNA.

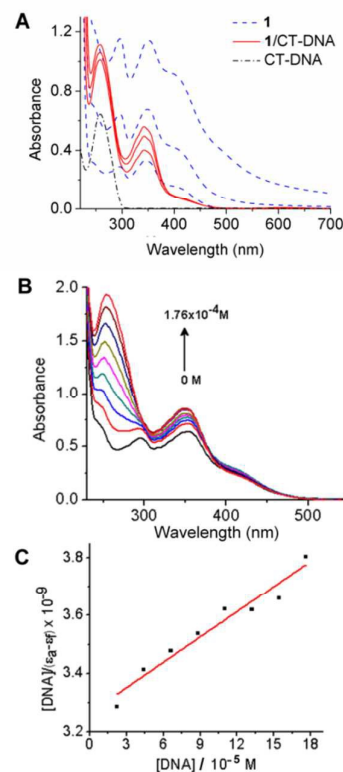


Fig. 7 Determination of binding constant by absorption titration of **1** with CT-DNA. (A) Absorption spectra of CT-DNA (8.81×10^{-7} M, ----CT-DNA), **1** (1, 3, and 6×10^{-5} M, ---complex **1**) and CT-DNA in presence **1**, 3, and 6×10^{-5} M of the complex (—1/CT-DNA). (B) Absorption spectra of **1** (3×10^{-5} M) without (0 M) and with CT-DNA at different concentrations (2.202, 4.405, 6.607, 8.81, 11.01, 13.21, 15.41 and 17.62×10^{-5} M); (C) Plot of $[\text{DNA}]/(\epsilon_a - \epsilon_f) \times 10^9$ versus $[\text{DNA}]$.

In the spectra of Zn(II)-complex/CT-DNA, the peak at 258 nm was also observed with an increase in absorption intensity, Fig. 7A (hyperchromism was calculated as -57%, -64% and -72%). The absorption intensity at 258 nm was increased due to exposition of purine and pyrimidine bases due to complex binding. In order to obtain information on affinity of **1** for CT-DNA, a spectroscopic titration of the solution of the complex with increasing concentration of CT-DNA was performed (Fig. 7B). The absorbance at 258 nm was monitored for each concentration of DNA. The intrinsic binding constant K_B of the complex (Fig. 7C) was calculated as $8.92 \times 10^4 \text{ M}^{-1}$ (for calculation details see experimental section). The value of binding constant was lower than reported for a classical intercalator, *i.e.* a range from 10^6 to 10^7 M^{-1} .⁶⁵ The value of K_B for **1** was comparable to those for other metal complexes,^{64,66} suggesting minor groove binding of **1**. The spectral changes that occur when **1** was added to CT-DNA, as well as the absence of isobestic points in these spectra, suggest that more than a single binding mode can occur.

In order to further investigate the binding mode, fluorescence analyses were performed. Upon excitation at $\pi \rightarrow \pi^*$ transitions either in DMSO or in the presence CT-DNA, **1** did not emit luminescence. Hence, indirect evidence for the binding mode was examined by fluorescent displacement experiments, carried out with two different dyes: ethidium bromide (EB), a typical DNA intercalator and Hoechst 33258 (H), a minor groove binder. It is known that EB interacts with CT-DNA in the intercalation mode with strong binding affinity.⁶⁷ The extent of the fluorescence quenching of EB by competitive displacement from DNA is a measure of the strength of the interaction between second molecule and DNA.⁶⁸ Binding of EB to CT-DNA was followed by excitation at 500 nm with maximum in fluorescence at 600 nm. The emission spectra of EB bound to CT-DNA in the absence and presence of **1** are given in Fig. 8. A continuous decrease was observed in fluorescence intensity at 600 nm for EB-CT-DNA for increasing concentration of **1** (up to 22 μM , see experimental section). It was shown that the complex quenches the fluorescence probe with the maximal decrease in the fluorescence intensity of the EB-CT-DNA by 18%, followed by saturation at high concentration of **1** (14 μM) (Fig. 8A and the inset). Fig. 8B shows that the obtained fluorescence quenching data gave a linear plot in accordance with the Stern-Volmer equation (6) (see experimental section). The fluorescence quenching constant (K_{sv}) value was calculated from the ratio of the slope to the intercept from the plot of I_0/I versus r (ratio of concentrations of complex **1** and CT-DNA, $r = [\mathbf{1}]/[\text{CT-DNA}]$) as $K_{sv} = 1.802$. The observed saturation at high concentrations of **1** indicated that **1** quenches the fluorescence of EB-CT-DNA by displacement of bound EB in a limited fraction of binding sites.

To further clarify the interaction of **1** with DNA, fluorescent displacement experiments with H dye were performed. H preferentially binds in the minor groove at A:T-rich sequences in B-DNA at the edges of four to five contiguous base pairs with nanomolar affinity.⁶⁹

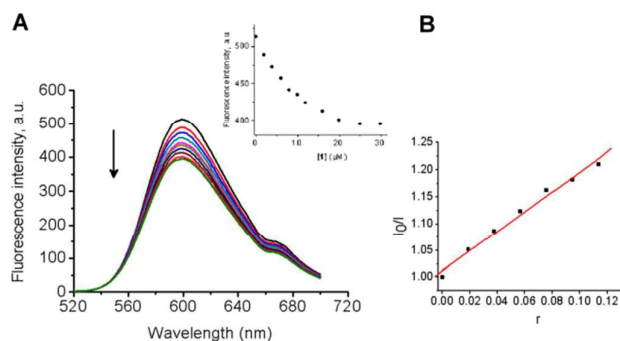


Fig. 8 Displacement of DNA-bound ethidium bromide (EB) by **1**. (A) Emission spectra ($\lambda_{\text{ex}} = 500 \text{ nm}$) of EB ($2.5 \times 10^{-5} \text{ M}$) bound to CT-DNA ($1 \times 10^{-4} \text{ M}$, top line) and quenching of EB-CT-DNA system by **1** at increasing concentrations ($0 - 3 \times 10^{-5} \text{ M}$, curves from top to bottom). The arrow shows that fluorescence intensity decreased with increasing concentration of the complex. The inset demonstrates the saturation of binding. (B) Fluorescence quenching curves of EB bound to CT-DNA at $\lambda_{\text{max}} = 600 \text{ nm}$ by **1**; $r = [\mathbf{1}]/[\text{CT-DNA}]$.

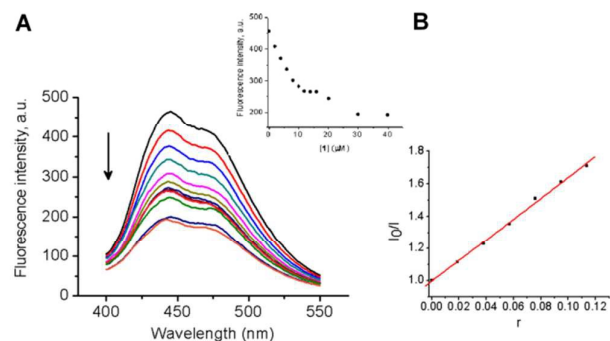


Fig. 9 Displacement of DNA-bound Hoechst 33258 (H) by **1**. (A) Emission spectra ($\lambda_{\text{ex}} = 350 \text{ nm}$) of H ($2.8 \times 10^{-5} \text{ M}$) bound to CT-DNA ($1 \times 10^{-4} \text{ M}$, top line) and quenching of H-CT-DNA system by **1** at increasing concentrations ($0 - 4 \times 10^{-5} \text{ M}$, curves from top to bottom). The arrow shows that fluorescence intensity decreased with increasing concentration of the complex. The inset demonstrates the saturation of binding. (B) Fluorescence quenching curves of H bound to CT-DNA at $\lambda_{\text{max}} = 440 \text{ nm}$ by **1**; $r = [\mathbf{1}]/[\text{CT-DNA}]$.

Also, an unspecific weaker binding at a high $[\text{H}]/[\text{DNAbp}]$ ratio have to be considered.⁷⁰ Fig. 9A shows the characteristic emission spectrum of H when it is bound to CT-DNA. The addition of **1** to CT-DNA caused appreciable reduction in the fluorescence intensity of H-CT-DNA system in concentration dependent way. The quenching of H-CT-DNA showed an initial saturation at 10 μM concentration of **1** (inset in Fig. 9A). It is important to note that the fluorescence intensity was reduced to nearly half of the initial value. The half-reciprocal plot of the quenching data according to Stern-Volmer equation resulted in a linear plot with a quenching constant $K_{sv} = 6.43$. The value of quenching constant K_{sv} was calculated from the ratio of the slope to the intercept from the plot of I_0/I versus r ($r = [\mathbf{1}]/[\text{CT-DNA}]$) (Fig. 9B). With increasing concentration of **1**, an additional decrease in fluorescence intensity was observed, followed by saturation in competitive displacement from H-CT-DNA system.

The obtained results of the extent of the fluorescence quenching of EB by competitive displacement from EB-CT-DNA

system and groove binder H from H–CT-DNA system demonstrated that **1** non-selectively binds to DNA, exhibiting both binding modes. Comparing K_{sv} values for the quenching fluorescence intensity by displacement it may be concluded that **1** was more efficient as a groove binder than as an intercalator. The results are in agreement with UV-Vis spectrophotometry data.

Considering that the electrostatic interaction between positively charged complex cation $[Zn(Hqasesc)_2]^{2+}$ and the negatively charged phosphate backbone may occur, with respect to the geometry of the complex, it can be concluded that optimal interaction can include partial intercalation of aromatic rings in the minor groove of double helix of CT-DNA. This mode of interaction with DNA by partial intercalation and specific minor groove binding was earlier described for bleomycins.⁷¹

Plasmid DNA interaction study

The ability of **1** to cleave double-stranded plasmid DNA in the absence of any reducing agents was investigated using an electrophoretic analysis. As it shown in Fig. 10 (lane 1), plasmid pUC19 consists mainly of supercoiled form FII and nicked form FI. DMSO did not show any effect on plasmid DNA in the performed experimental conditions (Fig. 10, lane 2). Upon addition of increasing concentration of **1** to the plasmid, a gradual diminishing of the supercoiled form FI and nicked form FII was observed (Fig. 10, lanes 3–6) and the forms disappeared at a much higher concentration of **1** (35 and 40 μ M, lanes 7 and 8, respectively). The possible multimer forms with very slow mobility were observed (remained at the start of run). The generation of the multimer was concentration dependent indicating that **1** does not possess nuclease activity. A possible cause for aggregation can be formation of multiple hydrogen bonds between the complex cation and phosphate moieties in the plasmid DNA. Such multiple hydrogen bonds were observed in the crystal structure between the complex cation and perchlorate anion, which as like phosphate, has a tetrahedral geometry.

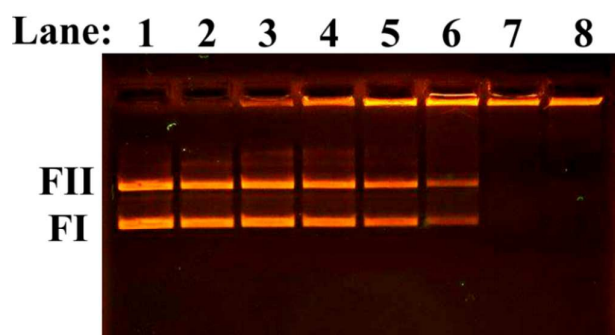


Fig. 10 Agarose gel electrophoresis of cleavage reaction of pUC19 by **1**. The cleavage reaction was investigated by incubation for 90 min of 512 ng plasmid in 20 μ L of 40 mM bicarbonate buffer (pH 8.4) at 37 $^{\circ}$ C, with different concentrations of **1**. Lane 1 – control plasmid pUC19; lane 2 plasmid pUC19 with DMSO (20% final); lanes 3–8: pUC19 with 0.015, 0.02, 0.025, 0.03, 0.035, and 0.04 mM concentration of **1**, respectively.

Interaction between **1** and human serum albumin (HSA)

The interaction between **1** and HSA has been studied by UV-Vis and fluorescence spectroscopy. UV-Vis spectra of HSA with increasing amounts of **1** showed blue λ_{max} shift (from 280 to 271 nm, Fig. 11A). Results indicate interaction between HSA and **1**, leading to changes in the protein structure upon ligand binding. The changes in fluorescence emission spectra of HSA with the increasing amount of **1** are shown on Fig. 11B.

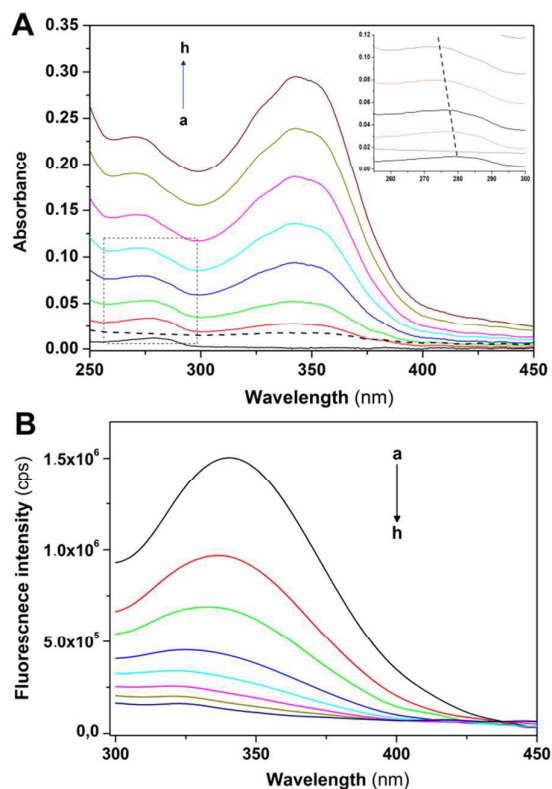


Fig. 11 Changes in UV-Vis absorption spectra (A) and fluorescence emission spectra (B) of HSA ($c = 5 \times 10^{-7}$ M) in PBS buffer (1 \times PBS, pH 7.35) upon addition of **1** in following concentrations ($\times 10^{-6}$ M): (a) 0.0; (b) 0.34; (c) 0.68; (d) 1.36; (e) 2.04; (f) 3.06; (g) 4.08; (h) 5.1. The UV-Vis absorption spectrum of pure complex **1** ($c = 5 \times 10^{-7}$ M) is represented with dashed line; magnified part of the original HSA spectrum around λ_{max} (280 nm) is embedded, with blue shift indicated with dashed line.

As the concentration of **1** increases, results may deviate from initial linearity due to instrumental inner filter effect.⁷² In order to overcome this problem, absorbance was measured at excitation (280 nm) and emission (340 nm) wavelengths, and fluorescence intensities corrected according to the Lakowicz equation⁷³ given in the experimental part. Corrected fluorescence intensities were used for further calculations.

Upon addition of increasing amount of **1**, significant decrease of HSA fluorescence intensity (fluorescence quenching) is observed, as well as the blue shift of the wavelength of maximum emission (340 nm). This shift indicates that the microenvironment around Trp214 is altered as HSA–**1** adduct is formed. In general, fluorescence quenching might be classified as static or dynamic. Dynamic quenching is highly dependent upon diffusion. Higher temperatures result

in faster diffusion and hence larger values for bimolecular quenching constant. On the other hand, higher temperatures will typically result in the dissociation of weakly bound complexes, and therefore decrease the bimolecular quenching constant in static process. Fluorescence quenching data were processed using Stern-Volmer equation⁷⁴ (for details see experimental part) in order to obtain K_{sv} and K_q , Stern-Volmer quenching constant and the quenching rate constant of a protein, respectively (Fig. S16, ESI). As can be seen from Table 4, K_{sv} decreases as temperature increases, indicating that the quenching mechanism is static. Another confirmation of static quenching mechanism is the value of K_q , which is higher than the maximum scatter collision quenching constant value ($2 \times 10^{10} \text{ M}^{-1} \text{ s}^{-1}$).⁷⁵

The quenching process was additionally analyzed using modified Stern-Volmer equation⁷³ in order to obtain the effective quenching constant, K_a , for the accessible fluorophores, and the fraction of accessible fluorophore f_a . Results are shown on Fig. S17 (ESI) and in Table 5.

Table 4. Results of Stern-Volmer plot at different temperatures (the average fluorescence lifetime $\tau_0 = 7.09 \text{ ns}$ for HSA). K_{sv} is obtained as a slope, while intercept is kept constant (= 1).

T (K)	$10^6 \times K_{sv} (\text{M}^{-1})$	$10^{14} \times K_q (\text{M}^{-1} \text{ s}^{-1})$	r^2
293	2.01±0.04	2.82	0.995
298	1.91±0.04	2.70	0.994
310	1.51±0.03	2.13	0.993

Table 5. Results of binding of **1** to HSA obtained using modified Stern-Volmer plot; thermodynamic parameters of binding are calculated using Van't Hoff equation.

T (K)	$10^6 \times K_a (\text{M}^{-1})$	f_a	r^2	ΔH (kJmol^{-1})	ΔG (kJmol^{-1})	ΔS ($\text{Jmol}^{-1}\text{K}^{-1}$)
293	1.50±0.03	0.973	0.999	-11.02	-34.64	80.75
298	1.44±0.02	0.972	0.998		-35.13	
310	1.18±0.01	0.946	0.990		-36.03	

The K_a is inversely correlated with temperature, which is in accordance with K_{sv} temperature dependency.

Thermodynamic binding parameters, enthalpy (ΔH) and entropy change (ΔS), for binding of a small molecule to a protein can be calculated according to Van't Hoff equation (given in the experimental section) by measuring the binding constants at several temperatures. Results are shown in Fig. S18 (ESI) and in Table 5. According to Ross' view,⁷⁶ signs and magnitudes of thermodynamic parameters for protein reactions can account for the main forces contributing to protein stability. From the thermodynamic stand-point, $\Delta H > 0$ and $\Delta S > 0$ implies a hydrophobic interaction, $\Delta H < 0$ and $\Delta S < 0$ reflects the van der Waals force or hydrogen bond formation and $\Delta H < 0$ and $\Delta S > 0$ suggest an electrostatic force. In our case, $\Delta H < 0$ and $\Delta S > 0$, indicates that the electrostatic forces are the main contributors to HSA-**1** binding.

When small molecules bind independently to a set of equivalent sites of a protein, the equilibrium between free and

bound molecules for the static quenching process is given by equation (1):⁷⁷

$$\log \frac{F_0 - F}{F} = \log K_b + n \log [Q] \quad (1)$$

where F_0 and F are the steady-state fluorescence intensities in the absence and presence of **1**; K_b is binding constant, n is the number of binding sites and $[Q]$ denotes the total concentration of quencher. Linear dependence is shown in Fig. S19 (ESI), and the results of linear fit are given in Table 6. As value of n is close to 1, it is suggested that **1** binds only to one binding site. The value of K_b is in order of 10^6 . These results, along with previously determined effective quenching constant K_a , suggest that **1** strongly binds to HSA, so it can be effectively carried and stored in the human body.

Table 6. Binding constants and the number of binding sites for the interaction of **1** with HSA at three temperatures.

T (K)	$\log K_b (\text{M}^{-1})$	n	r^2
293	5.52 ± 0.16	0.897	0.995
298	5.47 ± 0.18	0.892	0.994
310	5.73 ± 0.25	0.958	0.990

Fluorescence resonance energy transfer (FRET) is a non-destructive spectroscopic method that can give information about the distance and relative orientation of the donor (Trp 214, D) and acceptor fluorophore (interacting molecule, A). The resonance transfer is more efficient when spectral overlap of donor emission and acceptor absorption is large (Fig. S20, ESI). The distance between D and A, r , could be calculated using energy transfer efficiency, E ⁷³ (for calculation details see experimental part). We have calculated the overlap integral of the donor emission and the acceptor absorption spectra ($J = 5.87 \times 10^{-15} \text{ M}^{-1} \text{ cm}^3$, Fig. S20, ESI), the energy transfer efficiency ($E = 0.230$), the Förster's distance at which energy transfer is 50% efficient ($R_0 = 2.385 \text{ nm}$), and the D-A distance ($r = 3.098 \text{ nm}$). Since the distances between D and A are usually in the range 2–8 nm, and obtained r value obeys the condition $0.5R_0 < r < 1.5R_0$,⁷³ we may conclude that the energy transfer between HSA and **1** is highly feasible process.

Molecular docking of **1** with DNA and HSA

To examine the binding of zinc complex to DNA we used the DNA duplex of sequence d(CGCGAATTCGCG)₂ (for details see experimental section). Molecular docking gave conformations binding to minor and major groove, with slight preference to minor groove (Fig. S21, ESI). Conformations with lowest binding energy correspond to minor groove, and difference between lowest conformation and one bound to major groove has the value of $0.1 \text{ kcal mol}^{-1}$. No intercalating structures were found. The pattern of binding is presented in Fig. 12. The established interactions between **1** and DNA nucleotides are hydrogen bonds and aromatic interactions. This is expected, as **1** consists of coordinated groups that are hydrogen bond donors, particularly NH_2 groups. Aromatic systems from zinc

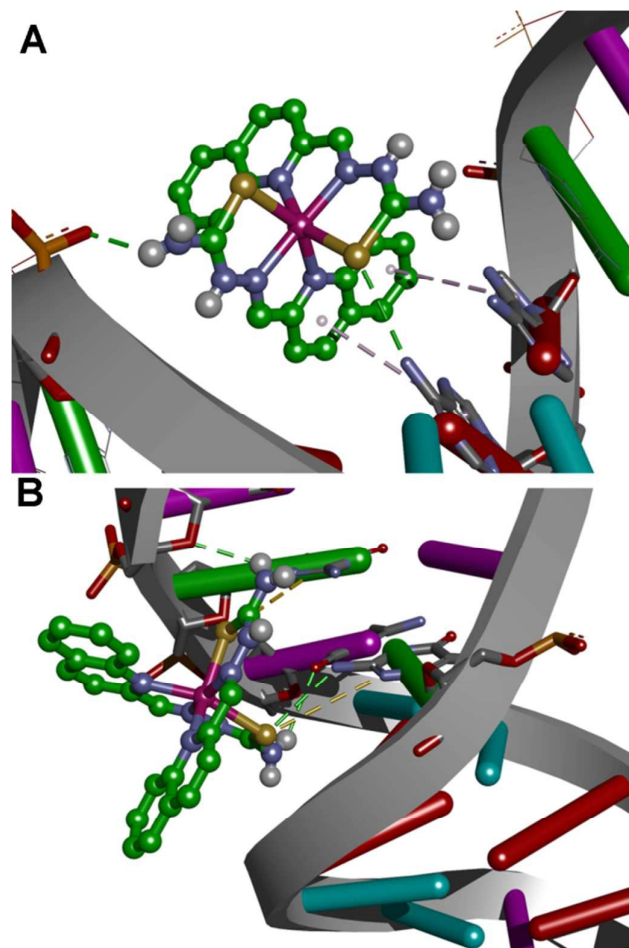


Fig. 12 Binding pattern of **1** to DNA with marked interactions: major groove (A) and minor groove (B). Color code: green - hydrogen bonds; grey - aromatic interactions; dark yellow - selenium- π interactions.

complex tend to form CH- π interactions with DNA bases, along with selenium (Se- π interactions), which can also form hydrogen bonds with bases. This is in accordance with experimental results, as reported that **1** has more affinity to minor groove than major, and measurements showed no significant intercalation.

The Zn(II) complex was docked into previously identified binding sites of HSA (PDB IDs 2BXD and 4L9Q, see experimental part for details), but obtained values of binding energies were not in accordance with experimental results, as they were too high or showing low binding affinity. Therefore we decided to search the whole conformational space of HSA (PDB ID 1BJ5) which gave an insight into other possible binding sites. According to reported thermodynamic properties of ligand binding, we selected one conformation that was in the best accordance with the experiment, at the same time having the lowest binding energy, with value $E_b = -36.38 \text{ kJ mol}^{-1}$. As presented in Fig. 13, the main electrostatic interaction is formed with Glu 354, having in mind that the complex cation is +2 charged and electrostatic effects are transmitted through organic ligands coordinated to Zn(II). Also, nitrogen atoms of

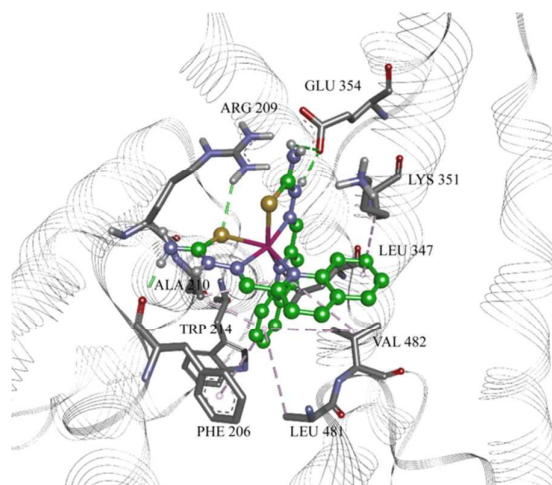


Fig. 13 The Zn(II) complex in binding site of HSA (PDB ID 1BJ5), with marked amino acid residues and interactions. Green: hydrogen bonds; grey: hydrophobic/aromatic interactions.

Arg 209 and Lys 351 and selenium atoms are sufficiently close, so the electrostatic interaction with partially positive hydrogen atoms on the residues cannot be neglected, and this is in accordance with reported $\Delta H < 0$. The rest of interactions are of hydrophobic type, CH- π and aromatic, including interaction of residues Leu 347, Phe 206, Ala 210, Val 482, Leu 481, and aliphatic chain of Lys 351 with aromatic rings of the ligand. This confirms the reported $\Delta S > 0$ value. Also, the reported binding site is not much away from earlier reported binding site II,⁷⁸ as it is close to Trp 214 (Fig.S22, ESI). The interactions and distances with the ligand are presented in Table S2 (ESI). According to the docking site results, binding affinity values and interactions, it can be concluded that this can be a binding site for the reported compound, and its high affinity to HAS can be explained.

Conclusions

A novel zinc(II) complex with 2-quinolinecarboxaldehyde selenosemicarbazone ligand was synthesized and characterized. Investigation of biological activity shows that both compounds are strong apoptosis inducers in THP-1 cells. The apoptotic induction is concentration-dependent and coincides with an arrest at the S phase of mitotic division, indicating that Hqasesc and **1** interfere with DNA replication. Results of DNA binding and DNA docking experiments confirm our hypothesis, revealing that **1** not selectively binds to DNA, but with a higher affinity for minor groove, with no significant intercalation. Therefore, lack of caspase-8 and -9 activation in THP-1 cells treated with **1** is consistent since apoptosis could be triggered here by caspase-2 cascade after inhibited DNA replication. On the other hand, both compounds display less activity on AsPC-1 cell line, which one could expect since those cells are mainly CSCs, being non differentiated and so more resistant to most conventional therapeutics. While Hqasesc in

AsPC-1 cells induces apoptosis only at the highest applied concentration, treatment with **1** shows a concentration-dependent apoptotic response, obviously not induced by DNA drug interaction, considering that treated cells are arrested in the G1-to-S phase, accompanied by an extensive caspase-8 and -9 activation. These results indicate that Hqasesc and **1** display cell phenotype specific activity, which is a desirable characteristic that might signify cytotoxicity on a wide spectrum of cancer types. Finally, high affinity of **1** for HSA implies a possible pharmacokinetic property. Unbound fraction of the drug in plasma may be the active form, also subjected to metabolic transformation and excretion. HSA-bound fraction of the drug may serve as a depository, slowly releasing it as unbound active form. High percentage of HSA-bound drug will than prolong its half-life, reducing its volume of distribution, and thus avoid possible interactions with other drugs that compete for binding to HSA.

Experimental section

Reagents and instrumentation

Selenosemicarbazide (98%) was obtained from Acros Organics (BVBA, Geel, Belgium). 2-Quinolincarboxaldehyde and zinc perchlorate hexahydrate were obtained from Aldrich (Sigma-Aldrich Chemie GmbH, Steinheim, Germany). All solvents (reagent grade) were obtained from commercial suppliers and used without further purification.

Elemental analyses (C, H, N) were performed by the standard micromethods using the ELEMENTARVario ELIII C.H.N.S=O analyzer. IR spectra were recorded on a Thermo Scientific Nicolet 6700 FT-IR spectrophotometer by the Attenuated Total Reflection (ATR) technique in the region 4000–350 cm⁻¹. Abbreviations used for IR spectra: vs, very strong; s, strong; m, medium; w, weak. Molar conductivity measurements were performed at ambient temperature (298 K) on the Crison Multimetric MM41. NMR spectral assignments and structural parameters were obtained by combined use of ¹H homonuclear spectroscopy (2D COSY and NOESY) and multinuclear proton-detected spectroscopy (2D HSQC, 2D HMBC). The NMR spectra were performed on Bruker Avance 500 equipped with broad-band direct probe. Chemical shifts are given on δ scale relative to tetramethylsilane (TMS) as internal standard for ¹H and ¹³C. Abbreviations used for NMR spectra: s, singlet; dd, doublet of doublets; ddd, double doublet. Cyclic voltammetric measurements were performed using an electrochemical system CH Instruments (USA). UV-Vis spectra for acidity constant determination were recorded on Thermo Scientific Evolution 60S spectrophotometer (Thermo Fisher Scientific Inc, Waltham, Massachusetts, USA) in 250–500 nm range. pH values were measured using CRISON pH-Burette 24 2S equipped with CRISON 50 29 micro-combined pH electrode (CRISON INSTRUMENTS, S.A. Spain). For DPPH scavenging activity, absorbance at 517 nm was measured using Thermo Scientific Appliskan. Pro-apoptotic activity was determined on Guava EasyCyteTM micro-capillary flow cytometer (EMD Millipore, Darmstadt, Germany) using InCyte®

software package (EMD Millipore, Cat. No. 0500-4120). UV-Vis spectra for DNA binding studies were recorded on a UV-1800 Shimadzu UV-Visible spectrometer operating from 200 to 800 nm in 1.0 cm quartz cells, while for fluorescence measurements a Thermo Scientific Lumina Fluorescence spectrometer (Finland) equipped with a 150 W xenon lamp was used. A Submarine Mini-gel Electrophoresis Unit (Hoeffer HE 33) with an EPS 300 power supply was used for DNA cleavage studies. The stained gel was illuminated under a UV transilluminator Vilber-Lourmat (France) at 312 nm and photographed with a Nikon Coolpix P340 Digital Camera through filter Deep Yellow 15 (Tiffen, USA). UV-Vis spectra for HSA binding studies were recorded on a Thermo Scientific Evolution 60S UV-Vis spectrophotometer, using quartz cell with 1.0 cm path length, while fluorescence measurements were performed on spectrofluorometer Fluoromax-4 Jobin Yvon (Horiba Scientific, Japan), equipped with Peltier element for temperature control and magnetic stirrer for cuvette, using quartz cell with 1 cm path length.

Synthesis of Hqasesc

The ligand was synthesized according to the reported procedure.¹⁴ Single crystals suitable for X-ray analysis were obtained by recrystallization of the crude product from EtOH. The chemical structure of Hqasesc was confirmed by elemental analysis, IR and NMR spectroscopy. These data are in good agreement with the data previously reported.¹⁴

Synthesis of [Zn(Hqasesc)₂](ClO₄)₂ × EtOH (**1**)

Into the solution of 2-quinolincarboxaldehyde (0.15 g, 0.96 mmol) and selenosemicarbazide (0.13 g, 0.96 mmol) in EtOH (20 mL), Zn(ClO₄)₂ × 6H₂O (0.18 g, 0.48 mmol) was added. The reaction mixture was refluxed for 30 min and cooled to ambient temperature. Dark red crystals of **1** were obtained from ethanolic solution, filtered off and washed with cold ethanol and ether. Yield: 0.28 g (66%). Found: C, 33.5; H, 3.1; N, 12.9. Calc. for C₂₄H₂₆Cl₂N₈O₉Se₂Zn: C, 33.3; H, 3.0; N, 13.0%. IR (ATR), $\nu_{\text{max}}/\text{cm}^{-1}$: 3434m (NH₂), 3297vs (NH), 3183vs (NH), 3077s (NH₂), 1617s (C=N), 1578s (NH), 1511m (CH), 1100vs (ClO₄⁻). $\Lambda_{\text{M}}(1 \times 10^{-3} \text{ M, EtOH})$: 72.0 $\Omega^{-1} \text{ cm}^2 \text{ mol}^{-1}$. ¹H NMR (500 MHz, DMSO, TMS) [ppm] δ : 12.56 (s, 1H, N3H), 9.28 (s, 1H, N4Hb), 9.14 (s, 1H, N4Ha), 8.86 (d, 1H, C4H, ³J_{4,3} = 8.8 Hz), 8.72 (d, 1H, C3H, ³J_{3,4} = 8.8 Hz), 8.38 (s, 1H, C9H), 8.19 (dd, 1H, C5H, ³J_{5,6} = 7.7 Hz, ⁴J_{5,7} = 1.1 Hz), 8.13 (dd, 1H, C8H, ³J_{8,7} = 8.5 Hz, ⁴J_{8,6} = 1.3 Hz), 8.01 (ddd, 1H, C7H, ³J_{7,8} = 8.5 Hz, ³J_{7,6} = 7.0 Hz, ⁴J_{7,5} = 1.1 Hz), 7.83 (ddd, 1H, C6H, ³J_{6,5} = 7.7 Hz, ³J_{6,7} = 7.0 Hz, ⁴J_{6,8} = 1.3 Hz). ¹³C NMR (126 MHz, DMSO, TMS) [ppm] δ : 175.86 (C10), 151.04 (C2), 142.42 (C4), 140.71 (C8a), 136.57 (C9), 133.28 (C7), 128.98 (C6), 128.77 (C5), 128.12 (C4a), 123.27 (C8), 119.23 (C3). Numbering of atoms used in NMR is given in Scheme S1 (ESI).

Direct syntheses of the **1** starting from zinc perchlorate and Hqasesc in EtOH afforded identical product as the template syntheses, but in a slightly lower yield.

X-ray crystallography

Single crystal X-ray diffraction was performed on an Oxford Diffraction Gemini S kappa geometry diffractometer, equipped with Mo $K\alpha$ radiation from a sealed tube source, and a Sapphire CCD detector. Data collection strategy calculation, data reduction, cell refinement and absorption correction were performed with the *CRYSTALISPRO*.⁷⁹ Structure was solved using *SHELXT*,⁸⁰ and refined with anisotropic displacement parameters for all non-hydrogen atoms using *SHELXL-2014*.⁸¹ Program *SHELXL*⁸² was used as graphical user interface for structure solution and refinement procedures. Hydrogen atoms bonded to carbon atoms were introduced in idealized positions and refined using riding model. Hydrogen atoms bonded to nitrogen atoms were located by difference Fourier synthesis, and refined using distance restraints with U_{iso} approximated by $1.2U_{eq}$ of the parent atoms in Hqasesc, whilst their free isotropic refinement was performed in 1. Hydroxyl group of the EtOH molecule in **1** showed positional disorder, which was modeled by refining occupational parameters, and applying distance restraints. Structure was validated using *PLATON*,⁸³ and Cambridge Structural Database (CSD) (v. 5.36, updates Nov. 2014)⁴⁵ using *MERCURY CSD*.⁴⁴

Crystallographic data for Hqasesc and **1** have been deposited with the Cambridge Crystallographic Data Centre as Supplementary publication Nos. CCDC 1413656 and 1413657, respectively. A copy of these data can be obtained, free of charge, via www.ccdc.cam.ac.uk/data_request/cif, or by emailing data_request@ccdc.cam.ac.uk.

Cyclic voltammetry

The cell (10 mL) consisted of three-electrode system, glassy carbon electrode (inner diameter of 3 mm; CHI 104) an Ag/AgCl (saturated KCl) reference electrode and Pt counter electrode. The potential was swept over the range from -2.0 to $+1.2$ V (vs. Ag/AgCl) at scan rate of 100 mVs⁻¹. Measurements were performed at room temperature with deaeration of solutions by passing a stream of nitrogen through the solution for 5 min prior to the measurement and then maintaining a blanket atmosphere of nitrogen over the solution during the measurement. The potentials were measured in 0.10 M [*n*-Bu₄N]PF₆/DMSO, and are quoted relative to Ag/AgCl reference electrode.

Determination of Hqasesc acidity constants

Acidity constants of Hqasesc were determined by spectrophotometric titration at $T = 298 \pm 1$ K. Working solution ($c = 3.1 \times 10^{-5}$ M) was prepared by dissolving accurately weighted dried substance in 5.00 mL of DMSO; 10 mM phosphate buffer (pH = 1.77, $I = 0.1$ M NaCl) was added up to 100.00 mL. pH Value was adjusted to 1.65 with conc. HCl. Small volume increments of 1 M KOH were added stepwise, until pH 11.91 was reached (total volume change at the end of the titration was lower than 2%). pH Value was continuously measured during titration and UV-Vis spectra recorded after pH value equilibration. UV-Vis spectra were recorded against the phosphate buffer as a blank. The pH electrode was

calibrated by standard CRISON buffer solutions (pH 4.01, 7.00, and 9.21). Acidity constants for Hqasesc were calculated according to transformed forms of classical spectrophotometric equations⁴³ which give linear dependence:

$$A = A_{H_2A^+} + \frac{A_{HA} - A}{[H_3O^+]} \times K_{a1} \quad (2)$$

$$(A - A_{HA}) \times 10^{pH} = \frac{A_{H_2A^+}}{K_{a1}} - \frac{1}{K_{a1}} A \quad (2a)$$

or

$$A = A_{A^-} + (A_{HA} - A) \times [H_3O^+] \times \frac{1}{K_{a2}} \quad (3)$$

or

$$(A - A_{HA}) \times 10^{-pH} = K_{a2} \times A_{A^-} - K_{a2} \times A \quad (3a)$$

where A represents absorbance of certain species (H_2A^+ , HA , or A^-) labeled in index, and K_{a1} and K_{a2} represent the first and second dissociation constant of Hqasesc, respectively.

Free radical scavenging antioxidant assay (DPPH method)

The proton donating ability was assayed using protocol for determination of radical scavenging activity.⁵² Compounds were dissolved in pure DMSO and were diluted into ten different concentrations. Commercially available free radical DPPH was dissolved in methanol at concentration 6.58×10^{-5} M. Into a 96-well microplate, 140 μ L of DPPH solution was loaded and 10 μ L DMSO solution of the tested compounds was added, or pure DMSO (10 μ L) as the control. The microplate was incubated for 30 min at 298 K in the dark and the absorbance was measured at 517 nm. All the measurements were carried out in triplicate. Scavenging activity of the compounds was calculated using the equation (4):

$$\text{Scavenging activity (\%)} = \frac{A_{control} - A_{sample}}{A_{control}} \times 100 \quad (4)$$

where A_{sample} and $A_{control}$ refer to the absorbances at 517 nm of DPPH in the sample and control solutions, respectively.

IC₅₀ values were calculated from the plotted graph of scavenging activity against the concentrations of the samples. IC₅₀ is defined as the total antioxidant concentration necessary to decrease the amount of the initial DPPH radical by 50%. IC₅₀ was calculated for all compounds based on the percentage of DPPH radicals scavenged. Ascorbic acid was used as the reference compound (positive control) with concentrations 50 to 500 μ g/mL.

Cell cultures

Acute monocytic leukemia cell line (THP-1, ATCC® TIB-202) and pancreatic adenocarcinoma cell line (AsPC-1, ATCC® CRL-1682) were maintained in RPMI-1640 (Life Technologies, 11875-093) and DMEM high glucose (Sigma-Aldrich, D5796) cell culture media, respectively. Both media were supplemented with 10% (v/v) fetal bovine serum (FBS, Gibco, Cat. No. 16000-036) and 1% (v/v) penicillin–streptomycin (10 000 units/mL and 10 000 μ g/mL, Gibco, Cat.No. 15140-130). Cells were kept at 37 °C in

atmosphere containing 5% (v/v) CO₂ during their exponential growth and during the course of experimental treatments.

The ligand Hqasesc and **1** were initially dissolved in DMSO to the stock concentration of 20 mM, whereas CDDP was dissolved in saline to the stock concentration of 5 mM. Further dilutions to the experimental concentrations applied on the cells have been done with RPMI-1640 or DMEM media immediately before each experiment, thus the final concentration of DMSO with cells treated with the highest applied concentration was 0.5% (v/v).

Determination of pro-apoptotic activity

THP-1 and AsPC-1 cells were seeded in 96 flat bottom well plates (Corning® Costar®, Cat. No. CLS3596) in a volume 0.1 mL, at a density of 10 000 per well. Since the THP-1 cells grow in suspension, experimental treatments started within 2 h after cells seeding, while plates with seeded AsPC-1 cells were left overnight to settle. Investigated compounds were added in a range of six concentrations. As controls, non-treated cells, cells treated with 0.5% DMSO, and cells treated with Celestrol (Enzo Life Sciences, Cat. No. ALX-350-332-M025) at 50 μM concentration were used.

After 24 h of incubation, THP-1 cells were centrifuged at RCF of 450 × *g* for 10 min, supernatants were discarded, and 0.1 mL of PBS was added to each well. Plates were placed on plate shaker for 3 min, afterwards Annexin-V-FITC (ImmunoTools, Cat. No. 31490013) and propidium iodide (PI, MiltenylBiotec, Cat. No. 130-093-233) were added in a volume of 3 μL per well, respectively, and incubated for 15 min in dark before cytometry analysis. Post incubation manipulation with AsPC-1 cells included trypsinization (200 μL of trypsin per well, Sigma-Aldrich, Cat. No. T3924). Subsequent steps with addition of PBS, Annexin-V and PI were the same as for THP-1 cells. Plates were analyzed on a flow cytometer. Cells were classified according to Annexin-V and PI labeling into viable (non-stained cells), pre-apoptotic cells (stained with Annexin-V only), cells in late phases of apoptosis (double stained cells), and necrotic cells (stained with PI only). After this read-out was ended, remaining cells were fixed in ethanol overnight at 4 °C, and afterwards stained with FxCycle™ PI/RNase Staining solution (Molecular Probes, Cat. No. F10797), and analyzed as described previously.⁸⁴

Calculation of ED₅₀ concentration

Separately for THP-1 and AsPC-1 cells, percent of Annexin-V labeled cells for each investigated concentration of compounds were summarized and maximum apoptotic response was normalized to 100%. Percent of apoptosis read-out for other concentrations were calculated as a proportion of the highest response. Such scaled apoptotic outcomes were plotted against concentrations and ED₅₀ concentration was calculated using asymmetric sigmoidal curve five-parameter logistic equation (GraphPad Prism 6 software). Determined ED₅₀ concentrations of both compounds were applied in further steps of this investigation.

Inhibition of caspase activity

THP-1 and AsPC1 cells were treated with investigated compounds at ED₅₀ concentration for 6 h with or without pan-caspase inhibitor Z-VAD-fmk (Promega, Cat. No. G7232). Previously, the proper concentration of Z-VAD-fmk that is non-toxic to cells during 6 h of incubation was determined (10 μM and 20 μM for THP-1 and AsPC-1 cell lines, respectively). As controls, non-treated cells, cells treated with Z-VAD-fmk only, and cells treated with ED₅₀ concentrations only were used. After incubation period had ended, plates with THP-1 and AsPC-1 treated cells were stained with Annexin-V/PI as described above, and analyzed on Guava EasyCyte™ cytometer. The percent of apoptosis inhibited by Z-VAD-fmk co-treatment was determined by the formula:

apoptosis inhibition, % = [1 – (% of apoptosis in A / % of apoptosis in B)] × 100, where A is the sample treated with both ED₅₀ and Z-VAD-fmk, while B is the corresponding sample treated with ED₅₀ only.

Evaluation of caspase-8 and -9 activities

THP-1 and AsPC1 cells were treated with investigated compounds at ED₅₀ concentration for 6 h. Afterwards activity of caspase-8 and -9 were assayed by means of Guava Caspase 9 SR and Caspase 8 FAM kit (EMD Millipore, Cat. No. 4500-0640), following instructions of the manufacturer. In acquired data cells were discriminated according to expression of green fluorescence (caspase-8), yellow fluorescence (caspase-9), or red fluorescence (7-AAD) as the following: live cells (not stained with either caspase nor 7-AAD), mid-stage apoptotic cells (cells stained with either caspase 8 or 9, but negative to 7-AAD), late stage apoptotic cells (cells stained with either of caspase 8 or 9 and with 7-AAD), necrotic cells (cells not stained with either caspase 8 nor 9, but positive for 7-AAD).

DNA binding experiments

Calf thymus DNA (lyophilized, highly polymerized, obtained from Serva, Heidelberg) (CT-DNA) was dissolved in Tris buffer (10 mM Tris-HCL pH 7.9) overnight at 4 °C. This stock solution (2.86 mg/mL) was stored at 4 °C and was stable for several days. A solution of CT-DNA in water gave a ratio of UV absorbance at 260 and 280 nm, A₂₆₀/A₂₈₀ of 1.89–2.01, indicating that DNA was sufficiently free of protein. The concentration of DNA (2.86 mg/mL) was determined from the UV absorbance at 260 nm using the extinction coefficient ε₂₆₀ = 6600 M⁻¹ cm⁻¹.⁸⁵ The complex was dissolved in DMSO in concentrations of 10 mM. This solution was used as stock solution.

UV-visible measurements. Reaction mixtures (1 mL in 40 mM bicarbonate buffer, pH 8.4) consisting of 1, 3 and 6 μL of the stock solution of **1** and 10 μL of the solution of CT-DNA were incubated at 37 °C for 90 min with occasional vortexing. The absorbance titrations were performed at a fixed concentration of **1** (30 μM) and gradually increasing concentration of double stranded CT-DNA (2.5, 5, 7.5, 10, 12.5, 15, 17.5 and 20 μL). The absorbance at 260 and 344 nm was monitored for each concentration of DNA. The binding constant *K*_b was determined using the equation (5).⁸⁶

$$[\text{DNA}] \times (\varepsilon_a - \varepsilon_f)^{-1} = [\text{DNA}] \times (\varepsilon_b - \varepsilon_f)^{-1} + K_b^{-1} \times (\varepsilon_b - \varepsilon_f)^{-1} \quad (5)$$

where ε_a , ε_f , ε_b are absorbance/[1], extinction coefficient of the free complex and the extinction coefficient of the bound compound, respectively. A plot of $[\text{DNA}]/(\varepsilon_a - \varepsilon_f)$ versus $[\text{DNA}]$ gave a slope and the intercept equal to $1/(\varepsilon_a - \varepsilon_f)$ and $(1/K_b)(1/(\varepsilon_b - \varepsilon_f))$, respectively. The binding constant K_b was calculated from the ratio of the slope to the intercept. The percentage of hyperchromicity or hypochromicity for the CT-DNA/[1] was determined from: $(\varepsilon_a - \varepsilon_f)/\varepsilon_f \times 100$.

Fluorescence measurements. The competitive interactions of **1** and the fluorescence probe (ethidium bromide – EB and Hoechst 33258 – H) with CT-DNA have been studied by measuring the change of fluorescence intensity of the probe–DNA solution after addition of **1**. Reaction mixtures containing 100 μM of CT-DNA (calculated per phosphate) in 1 mL of 40 mM bicarbonate solution (pH 8.4) were pretreated with 1 μL of the probe solution (25 μM of EB and 28 μM of H at final concentrations) for 20 min and the mixture was analyzed by fluorescence measurement. Then the gradually increasing concentrations of the complex (2, 4, 6, 8, 10, 12, 16, 20, 25, 30 and 40 μM final concentrations) were successively added and the change in the fluorescence intensity was measured. The slits on the excitation and emission beams were fixed at 10 nm. All measurements were performed by excitation at 500 nm in the range 520–700 nm for EB and by excitation at 350 nm in the range 390–600 nm for H. The control was EB–CT-DNA solution and H–CT-DNA solution, respectively. The complex did not have fluorescence under applied conditions. The obtained fluorescence quenching data were analyzed according to the Stern–Volmer equation (6):⁷³

$$\frac{I_0}{I} = 1 + K_{sv} [Q] \quad (6)$$

where I_0 and I represent the fluorescence intensities of probe–CT-DNA in absence and presence of **1**, respectively, K_{sv} is quenching constant and $[Q]$ is the concentration ratio of the complex to DNA ($[1]/[\text{CT-DNA}]$). The K_{sv} value is calculated from the ratio of the slope to the intercept from the plot of I_0/I versus $[Q]$.

DNA cleavage experiments

For DNA cleavage experiments the plasmid pUC19 (2686 bp, purchased from Sigma-Aldrich, USA) was prepared by its transformation in chemically competent cells *Escherichia coli* strain XL1 blue. Amplification of the clone was done according to the protocol for growing *E. coli* culture overnight in LB medium at 37 °C⁸⁷ and purification was performed using Qiagen Plasmid plus Maxi kit. Finally, DNA was eluted in 10 mM Tris-HCl buffer and stored at –20 °C. The concentration of plasmid DNA (512 ng μL^{-1}) was determined by measuring the absorbance of the DNA-containing solution at 260 nm. One optical unit corresponds to 50 $\mu\text{g mL}^{-1}$ of double stranded DNA.

The cleavage reaction of supercoiled pUC19 DNA by different concentration of **1** was investigated by incubation of 512 ng of plasmid in a 20 μL reaction mixture in 40 mM bicarbonate buffer (pH 8.4) at 37 °C, for 90 min. The reaction

mixtures were vortexed from time to time. The reaction was terminated by short centrifugation at RCF of 6708 $\times g$ and addition of 5 μL of loading buffer [0.25% bromophenol blue, 0.25% xylene cyanol FF and 30% glycerol in TAE buffer, pH 8.24 (40 mM Tris-acetate, 1 mM EDTA)]. The samples were subjected to electrophoresis on 1% agarose gel (Amersham Pharmacia-Biotech, Inc) prepared in TAE buffer pH 8.24. The electrophoresis was performed at a constant voltage (80 V) until bromophenol blue had passed through 75% of the gel. After electrophoresis, the gel was stained for 30 min by soaking it in an aqueous ethidium bromide solution (0.5 $\mu\text{g mL}^{-1}$).

HSA binding experiments

Fatty acid free HSA (< 0.007% fatty acids, $M_w = 66478$ Da) was purchased from Sigma, as well as potassium dihydrogen phosphate, disodium hydrogen phosphate, sodium chloride and potassium chloride used for 1 \times PBS preparation. Stock solution of HSA ($c = 2.78 \times 10^{-3}$ M) was prepared by dissolving accurately weighed mass of commercially available lyophilized HSA in freshly prepared 1 \times PBS (pH = 7.35), and kept in freezer in 100 μL portions. Stock solution of **1** ($c = 6.36 \times 10^{-4}$ M) was prepared by dissolving a proper amount of substance in DMSO. For HSA–**1** interaction studies, HSA solution was freshly prepared from the stock by dilution with PBS buffer (HSA concentration was kept constant, $c = 5 \times 10^{-7}$ M), and titrated with small volume increments of **1** stock solution (to avoid large sample dilution). The complex was added in 0.7, 1.4, 2.8, 4.2, 6.3, 8.4 and 10.5 molar equivalents. After each aliquot addition, system was stirred and left to equilibrate for 15 min before UV-Vis absorption and fluorescence emission spectra recording. After last equivalent, total DMSO did not exceed 2% in volume. It was previously shown that addition of 15% of DMSO did not induce structural changes in bovine serum albumin, a protein structurally similar to HSA.⁸⁸ Therefore, it is unlikely that the conformation of HSA was changed with the level of DMSO used in this study. Millipore water was used for all aqueous solutions. All UV-Vis spectra were recorded against the corresponding blank (PBS) in the 250–450 nm wavelength range at room temperature.

Before recording of fluorescence spectrum, diluted HSA solution was ultrafiltrated using filters with 0.23 μm pore size. An excitation wavelength was 280 nm, with 5 nm slits; emission spectra were recorded in 300–450 nm wavelength range, with 5 nm slits, and 0.1 s integration time. Background PBS signal was subtracted from each spectrum. In order to remove instrumental inner filter effect, the absorbances were measured at the excitation (280 nm) and emission (340 nm) wavelengths, and fluorescence intensities corrected according to the Lakowicz equation (7):⁷³

$$F_{corr} = F_{obs} \times 10^{\frac{A_{ex} + A_{em}}{2}} \quad (7)$$

where F_{corr} and F_{obs} are corrected and observed fluorescence intensities, and A_{ex} and A_{em} are absorbances at the excitation and emission wavelengths, respectively.

Fluorescence quenching data were processed using the Stern-Volmer equation (8):⁷³

$$\frac{F_0}{F} = 1 + K_{sv}[Q] = 1 + K_q\tau_0[Q] \quad (8)$$

where F_0 and F represents HSA fluorescence intensities in absence (F_0) and in presence of the quencher (F), K_{sv} and K_q are Stern-Volmer quenching constant and the quenching rate constant of protein, respectively, τ_0 is the average fluorescence lifetime (7.09 ns for HSA),⁷⁴ and $[Q]$ is the concentration of the quencher (1).

The quenching process was additionally analyzed using a modified Stern-Volmer equation (9):⁷³

$$\frac{F_0}{\Delta F} = \frac{1}{f_a K_a} \frac{1}{[Q]} + \frac{1}{f_a} \quad (9)$$

where ΔF is the difference in fluorescence intensity of HSA in the absence (F_0) and in the presence of the quencher at concentration $[Q]$. K_a represents the effective quenching constant for the accessible fluorophores, and f_a is the fraction of accessible fluorophore.

Thermodynamic parameters of binding, the enthalpy (ΔH) and entropy change (ΔS), during the binding of **1** to HSA were determined by measuring the binding constants at several temperatures, and following the Van't Hoff equation (10):

$$\ln K_o = -\frac{\Delta H}{RT} + \frac{\Delta S}{R} \quad (10)$$

where R is the universal gas constant, T is the temperature (in K), and K_o is the effective quenching constant at the corresponding temperature.

The distance between donor and acceptor, r , was calculated using equation (11) for energy transfer efficiency, E :⁷³

$$E = 1 - \frac{F}{F_0} = \frac{R_0^6}{R_0^6 + r^6} \quad (11)$$

where R_0 is called the Förster's distance, and represents the distance at which energy transfer is 50% efficient. R_0 is calculated according to equation (12):

$$R_0^6 = 8.79 \times 10^{-25} \kappa^2 n^{-4} \phi J \quad (12)$$

where κ^2 stands for the spatial orientation factor of the dipole, n is a refractive index of the medium, ϕ is the donor fluorescence quantum yield, and J is the overlap integral of the donor emission and the acceptor absorption spectra. The overlap integral, J , can be calculated according to equation (13):

$$J = \frac{\int_0^\infty F(\lambda)\epsilon(\lambda)\lambda^4 d\lambda}{\int_0^\infty F(\lambda)d\lambda} \quad (13)$$

where $F(\lambda)$ is fluorescence intensity (corrected for inner filter effect) of the donor in the wavelength of interest (in this case 300–450 nm) and ϵ is specific molar absorptivity of acceptor at certain wavelength. In the present study, $\kappa^2=2/3$ (for randomly oriented dipoles), $n = 1.336$, and $\phi = 0.118$ were used.⁸⁹

Computational details

Theoretical IR spectrum of 1. The geometry of **1** was optimized and vibrational frequencies were calculated at B97D⁹⁰ / TZVP^{91,92} level of theory in Gaussian 09, Revision D.01 software.⁹³ IR spectrum was visualized using GaussView 5,⁹⁴ and corresponding data were exported as text file in the range 0–4000 cm^{-1} with step size 1 cm^{-1} .

Molecular docking studies. Two randomly chosen X-ray crystal structures of dodecamer d(CGCGAATTCGCG)₂, PDB ID: 3U2N⁹⁵ and PDB ID: 4U8A,⁹⁶ and three HSA structures, PDB IDs: 1BJ5,⁹⁷ 2BXD⁹⁸ and 4L9Q,⁹⁹ were obtained from the Protein Data Bank (<http://www.rcsb.org/pdb>). The active sites were identified according to positions of crystallized ligands in the PDB structures. Ligands were removed, as well as water and ions and structures were prepared for docking using Autodock Tools 1.5.6.^{100,101} Docking was carried in Autodock Vina 1.1.2.¹⁰² Grid box size was set to 24 × 24 × 24 Å and exhaustiveness to 250. All calculations were carried on PARADOX computer cluster (Scientific Computing Laboratory of the Institute of Physics, Belgrade, Serbia). Hqsesc and **1** were prepared using X-ray determined coordinates, with Gasteiger charge correction done with Chimera program,¹⁰³ as no charges were assigned for selenium atoms.

Acknowledgements

The authors acknowledge networking support by the COST Action CM1106 StemChem – “Chemical Approaches to Targeting Drug Resistance in Cancer Stem Cells”. The work was funded by the Ministry of Education, Science and Technological Development of the Republic of Serbia (Grants 172055 and 172013). PARADOX computer cluster is supported in part by the Ministry of Education, Science and Technological Development of the Republic of Serbia (No. 171017) and by the European Commission under the FP7 projects (HP-SEE, PRACE-1IP, PRACE-2IP, EGI-InSPIRE).

References

- 1 T.S. Lobana, R. Sharma, G. Bawa and S. Khanna, *Coord. Chem. Rev.*, 2009, **253**, 977–1055.
- 2 J.S. Casas, M.S. Garcia-Tasende and J. Sordo, *Coord. Chem. Rev.*, 2000, **209**, 197–261.
- 3 H. Beraldo and D. Gambino, *Mini Rev. Med. Chem.*, 2004, **4**, 159–165.
- 4 D.S. Kalinowski, P. Quach and D.R. Richardson, *Future Med. Chem.*, 2009, **1**, 1143–1151.
- 5 N.S.H.N. Moorthy, N.M.F.S.A. Cerqueira, M.J. Ramos and P.A. Fernandes, *Recent Pat. Anticancer Drug Discov.*, 2013, **8**, 168–182.
- 6 G. Pelosi, *Open Crystallography Journal*, 2010, **3**, 16–28.

- 7 N.S.H.N. Moorthy, N.M.F.S.A. Cerqueira, M.J. Ramos and P.A. Fernandes, *Mini Rev. Med. Chem.*, 2013, **13**, 1862–1872.
- 8 B. Shakya, P.N. Yadav, J. Ueda and S. Awale, *Bioorg. Med. Chem. Lett.*, 2014, **24**, 458–461.
- 9 T.A. Yousef, G.M. Abu El-Reash, O.A. El-Gammal and S.F. Ahmed, *Polyhedron*, 2014, **81**, 749–763.
- 10 A.Y. Lukmantara, D.S. Kalinowski, N. Kumar and D.R. Richardson, *J. Inorg. Biochem.*, 2014, **141**, 43–54.
- 11 C. Gan, J. Cui, S. Su, Q. Lin, L. Jia, L. Fan and Y. Huang, *Steroids*, 2014, **87**, 99–107.
- 12 A. Mrozek-Wilczkiewicz, M. Serda, R. Musiol, G. Malecki, A. Szurko, A. Muchowicz, J. Golab, A. Ratuszna and J. Polanski, *ACS Med. Chem. Lett.*, 2014, **5**, 336–339.
- 13 M.A. Bhat, A. Al-Dhfyhan, A.A. Khan, N. Al-Harbi, P.S. Manogaran, A.M. Alanazi, H.K. Fun and M.A. Al-Omar, *Bioorg. Med. Chem. Lett.*, 2015, **25**, 83–87.
- 14 N. Filipović, N. Polović, B. Rašković, S. Misirlić-Denčić, M. Dulović, M. Savić, M. Nikšić, D. Mitić, K. Anđelković and T. Todorović, *Monatsh. Chem.*, 2014, **145**, 1089–1099.
- 15 A. Molter, J. Rust, C.W. Lehmann, G. Deepa, P. Chiba and F. Mohr, *Dalton Trans.*, 2011, **40**, 9810–9820.
- 16 A. Molter, G.N. Kaluderović, H. Kommera, R. Paschke, T. Langer, R. Pöttgen and F. Mohr, *J. Organomet. Chem.*, 2012, **70**, 80–86.
- 17 V. Zaharia, A. Ignat, B. Ngameni, V. Kuete, M.L. Mounang, C.N. Fokunang, M. Vasilescu, N. Palibroda, C. Cristea, L. Silaghi-Dumitrescu and B.T. Ngadjui, *Med. Chem. Res.*, 2013, **22**, 5670–5679.
- 18 H. Shen, H. Zhu, M. Song, Y. Tian, Y. Huang, H. Zheng, R. Cao, J. Lin, Z. Bi and W. Zhong, *BMC Cancer*, 2014, **14**, 629–639.
- 19 M.D. Revenko, V.I. Prisacari, A.V. Dizdari, E.F. Stratulat, I.D. Corja and L.M. Proca, *Pharm. Chem. J.*, 2011, **45**, 351–354.
- 20 K.C. Agrawal, B.A. Booth, R.L. Michaud, E.C. Moore and A.C. Sartorelli, *Biochem. Pharmacol.*, 1974, **23**, 2421–2429.
- 21 C.R. Kowol, R. Eichinger, M.A. Jakupc, M. Galanski, V.B. Arion and B.K. Keppler, *J. Inorg. Biochem.*, 2007, **100**, 1946–1957.
- 22 C. Pizzo, P. Faral-Tello, G. Salinas, M. Flo, C. Robello, P. Wipfe and S.G. Mahler, *Med. Chem. Commun.*, 2012, **3**, 362–368.
- 23 S.R. Turk, C.Jr. Shipman and J.C. Drach, *J. Gen. Virol.*, 1986, **67**, 1625–1632.
- 24 V. Calcaterra, O. Lopez, J.G. Fernandez-Bolanos, G.B. Plata and J.M. Padron, *Eur. J. Med. Chem.*, 2015, **94**, 63–72.
- 25 T.R. Todorović, A. Bacchi, G. Pelizzi, N.O. Juranić, D.M. Sladić, I.D. Brčeski and K.K. Anđelković, *Inorg. Chem. Commun.*, 2006, **9**, 862–865.
- 26 T.R. Todorović, A. Bacchi, N.O. Juranić, D.M. Sladić, G. Pelizzi, T.T. Božić, N.R. Filipović and K.K. Anđelković, *Polyhedron*, 2007, **26**, 3428–3436.
- 27 S. Bjelogrić, T. Todorović, A. Bacchi, M. Zec, D. Sladić, T. Srdić-Rajić, D. Radanović, S. Radulović, G. Pelizzi and K. Anđelković, *J. Inorg. Biochem.*, 2010, **104**, 673–682.
- 28 N. Gligorijević, T. Todorović, S. Radulović, D. Sladić, N. Filipović, D. Gođevac, D. Jeremić and K. Anđelković, *Eur. J. Med. Chem.*, 2009, **44**, 1623–1629.
- 29 T. Srdić-Rajić, M. Zec, T. Todorović, K. Anđelković and S. Radulović, *Eur. J. Med. Chem.*, 2011, **46**, 3734–3747.
- 30 M. Zec, T. Srdić-Rajić, A. Krivokuća, R. Janković, T. Todorović, K. Anđelković and S. Radulović, *Med. Chem.*, 2014, **10**, 759–771.
- 31 M. Zec, T. Srdić-Rajić, A. Konić-Ristić, T. Todorović, K. Anđelković, I. Filipović-Ljesković and S. Radulović, *Anticancer Agents Med. Chem.*, 2014, **10**, 1071–1080.
- 32 P.A. Sotiropoulou, M.S. Christodoulou, A. Silvani, C. Herold-Mende and D. Passarella, *Drug Discov. Today*, 2014, **19**, 1547–1562.
- 33 J.P. Thiery, H. Acloque, R.Y. Huang and M.A. Nieto, *Cell*, 2009, **139**, 871–890.
- 34 B. Beck and C. Blanpain, *Nat. Rev. Cancer*, 2013, **13**, 727–738.
- 35 F.H. Sarkar, Y. Li, Z. Wang and D. Kong, *Minerva Chir.*, 2009, **64**, 489–500.
- 36 T. Arumugam, V. Ramachandran, K.F. Fournier, H. Wang, L. Marquis and J.L. Abbruzzese, *Cancer Res.*, 2009, **69**, 5820–5828.
- 37 D. Kovala-Demertzi, P.N. Yadav, J. Wiecek, S. Skoulika, T. Varadinova and M.A. Demertzis, *J. Inorg. Biochem.*, 2006, **100**, 1558–1567.
- 38 D. Kovala-Demertzi, A. Alexandratos, A. Papageorgiou, P.N. Yadav, P. Dalezis and M.A. Demertzis, *Polyhedron*, 2008, **27**, 2731–2738.
- 39 C.R. Kowol, E. Reisner, I. Chiorescu, V.B. Arion, M. Galanski, D.V. Deubel and B.K. Keppler, *Inorg. Chem.*, 2008, **47**, 11032–11047.
- 40 E. Lopez-Torres, M.A. Mendiola, J. Rodriguez-Procopio, M.T. Sevilla, E. Colacio, J.M. Moreno and I. Sobrados, *Inorg. Chim. Acta*, 2001, **323**, 130–138.
- 41 J. Wang, *Analytical Electrochemistry*, Wiley-VCH, New York, 2nd edn., 2000, p. 34.
- 42 P.S. Zhao, H.Y. Wang, J. Song and L.D. Lu, *Struct. Chem.*, 2010, **21**, 977–987.
- 43 A. Albert and E. P. Serjeant, *The determination of Ionization constants*, Chapman and Hall, London, 2nd edn., 1971, p. 44.
- 44 C.F. Macrae, I.J. Bruno, J.A. Chisholm, P.R. Edgington, P. McCabe, E. Pidcock, L. Rodriguez-Monge, R. Taylor, J. van de Streek and P. A. Wood, *J. Appl. Crystallogr.*, 2008, **41**, 466–470.
- 45 F.H. Allen, *Acta Crystallogr.*, 2002, **B58**, 380–388.
- 46 T.R. Todorović, A. Bacchi, D.M. Sladić, N.M. Todorović, T.T. Božić, D.D. Radanović, N.R. Filipović, G. Pelizzi and K.K. Anđelković, *Inorg. Chim. Acta*, 2009, **362**, 3813–3820.
- 47 E. Manoj and M.R.P. Kurup, *Polyhedron*, 2008, **27**, 275–282.
- 48 X. Fan, J. Dong, R. Min, Y. Chen, X. Yi, J. Zhou and S. Zhang, *J. Coord. Chem.*, 2013, **66**, 4268–4279.
- 49 S. Zhang, J. Dong, X. Fan, Y. Chen and J. Zhou, *J. Coord. Chem.*, 2012, **65**, 3098–3110.
- 50 D.X. West, P.M. Ahrweiler, G. Ertem, J.P. Scovill, D.L. Klayman, J.L. Flippen-Anderson, R. Gilardi, C. George and L.K. Pannell, *Transition Met. Chem.*, 1985, **10**, 264–270.
- 51 M.T. Zimmerman, C.A. Bayse, R.R. Ramoutar and J.L. Brumaghim, *J. Inorg. Biochem.*, 2015, **145**, 30–40.
- 52 R.L. Prior, X. Wu and K. Schaich, *J. Agric. Food Chem.*, 2005, **53**, 4290–4302.
- 53 L. Galluzzi, I. Vitale, J.M. Abrams, E.S. Alnemri, E.H. Baehrecke, M.V. Blagosklonny, T.M. Dawson, V.L. Dawson, W.S. El-Deiry, S. Fulda, E. Gottlieb, D.R. Green, M.O. Hengartner, O. Kepp, R.A. Knight, S. Kumar, S.A. Lipton, X. Lu, F. Madeo, W. Malorni, P. Mehlen, G. Nuñez, M.E. Peter, M. Piacentini, D.C. Rubinsztein, Y. Shi, H.U. Simon, P. Vandenabeele, E. White, J. Yuan, B. Zhivotovsky, G. Melino and G. Kroemer, *Cell Death Differ.*, 2012, **19**, 107–120.
- 54 S.H. Lee, X.W. Meng, K.S. Flatten, D.A. Loegering and S.H. Kaufmann, *Cell Death Differ.*, 2013, **20**, 64–76.
- 55 D.V. Krysko, T. Vanden Berghe, K. D'Herde and P. Vandenabeele, *Methods*, 2008, **44**, 205–221.
- 56 G. Kroemer and S.J. Martin, *Nat. Med.*, 2005, **11**, 725–730.
- 57 D.R. McIlwain, T. Berger and T.W. Mak, *Cold Spring Harbor Perspect. Biol.*, 2013, **5**, a008656.
- 58 J. Puccini, L. Dorstyn and S. Kumar, *Cell Death Differ.*, 2013, **20**, 1133–1139.
- 59 A. Oleksi, A.G. Blanco, R. Boer, J. Usón, J. Aymamí, A. Rodger, M.J. Hannon and M. Coll, *Angew. Chem. Int. Ed.*, 2006, **45**, 1227–1231.
- 60 A. Terenzi, G. Barone, A. Silvestri, A.M. Giuliani, A. Ruggirello and V.T. Liveri, *J. Inorg. Chem.*, 2009, **103**, 1–9.

- 61 R. Eshkourfu, B. Čobeljić, M. Vujčić, I. Turel, A. Pevec, K. Sepčić, M. Zec, S. Radulović, T. Srdić-Radić, D. Mitić, K. Andjelković and D. Sladić, *J. Inorg. Biochem.*, 2011, **105**, 1196–1203.
- 62 C.Y. Gao, X. Qiao, Z.Y. Ma, Z.G. Wang, J. Lu, J.L. Tian, J.Y. Xu and S.P. Yan, *Dalton Trans.*, 2012, **41**, 12220–12232.
- 63 Z. Jannesari, H. Hadadzadeh, Z. Amirghofran, J. Simpson, T. Khayamian and B. Maleki, *Spectrochim. Acta A Mol. Biomol. Spectrosc.*, 2015, **136**, 1119–1133.
- 64 C. Icel and V.T. Yilmaz, *J. Photochem. Photobiol. B*, 2014, **130**, 115–121.
- 65 M. Cory, D.D. Mckee, J. Kagan, D.W. Henry and J.A. Miller, *J. Am. Chem. Soc.*, 1985, **107**, 2528–2536.
- 66 J. Wang, L. Shuai, X. Xiao, Y. Zeng, Z. Li and T. Matsumura-Inoue, *J. Inorg. Biochem.*, 2005, **99**, 883–885.
- 67 N.C. Garbett, N.B. Hammond and D.E. Graves, *Biophys. J.*, 2004, **87**, 3974–3981.
- 68 Y. Shi, C. Guo, Y. Sun, Z. Liu, F. Xu, Y. Zhang, Z. Wen and Z. Li, *Biomacromolecules*, 2011, **12**, 797–803.
- 69 F.G. Loontjens, P. Regenfass, A. Zechel, L. Dumortier and R.M. Clegg, *Biochemistry-US*, 1990, **29**, 9029–9039.
- 70 A. Adhikary, V. Buschmann, C. Müller and M. Sauer, *Nucleic Acids Res.*, 2003, **31**, 2178–2186.
- 71 J. Chen and J. Stubbe, *Curr. Opin. Chem. Biol.*, 2004, **8**, 175–181.
- 72 B. Birdsall, R.W. King, M.R. Wheeler, C.A. Lewis, S.R. Goode, R.B. Dunlap and G.C.K. Roberts, *Anal. Biochem.*, 1983, **132**, 353–361.
- 73 J.R. Lakowicz, *Principles of Fluorescence Spectroscopy*, Springer Science Business Media, New York, USA, 3rd edn., 2006, pp. 11, 56, 289.
- 74 M. Amiri, K. Jankeje and J.R. Albani, *J. Fluoresc.*, 2010, **20**, 651–656.
- 75 M.R. Eftink and C.A. Ghiron, *Anal. Biochem.*, 1981, **114**, 199–227.
- 76 P.D. Ross and S. Subramanian, *Biochemistry-US*, 1981, **20**, 3096–3102.
- 77 Y. Hu, Y. Liu, J. Wang, X. Xiao and S. Qu, *J. Pharm. Biomed. Anal.*, 2004, **36**, 915–919.
- 78 G. Sudlow, D.J. Birkett and D.N. Wade, *Mol. Pharmacol.*, 1975, **11**, 824–832.
- 79 CrysAlisPro Software system, Agilent Technologies UK Ltd., Oxford, 2014.
- 80 G.M. Sheldrick, *Acta Crystallogr., Sect. A*, 2015, **71**, 3–8.
- 81 G.M. Sheldrick, *Acta Crystallogr., Sect. C*, 2015, **71**, 3–8.
- 82 C.B. Hübschle, G.M. Sheldrick and B. Dittrich, *J. Appl. Crystallogr.*, 2011, **44**, 1281–1284.
- 83 A.L. Spek, *Acta Crystallogr., Sect. D*, 2009, **65**, 148–155.
- 84 S. Léonce, V. Pérez, S. Lambel, D. Peyroulan, F. Tillequin, S. Michel, M. Koch, B. Pfeiffer, G. Atassi, J.A. Hickman and A. Pierré, *Mol. Pharmacol.*, 2001, **60**, 1383–1391.
- 85 M.E. Reichmann, S.A. Rice, C.A. Thomas and P. Doty, *J. Am. Chem. Soc.*, 1954, **76**, 3047–3053.
- 86 R. Vijayalakshmi, M. Kanthimathi, V. Subramanian and B. Unni Nair, *Biochem. Biophys. Res. Commun.*, 2000, **271**, 731–734.
- 87 J. Sambrook, E.F. Fritsch and T. Maniatis, *Molecular Cloning: a Laboratory Manual*, Cold Spring Harbor Laboratory Press, USA, 2nd edn., 1989, pp. 133–134.
- 88 B. Ojha and G. Das, *J. Phys. Chem. B*, 2010, **114**, 3979–3986.
- 89 F.L. Cui, J. Fan, J.P. Li and Z.D. Hu, *Bioorg. Med. Chem.*, 2004, **12**, 151–157.
- 90 S. Grimme, *J. Comput. Chem.*, 2006, **27**, 1787–1799.
- 91 A. Schaefer, H. Horn and R. Ahlrichs, *J. Chem. Phys.*, 1992, **97**, 2571–2577.
- 92 A. Schaefer, C. Huber and R. Ahlrichs, *J. Chem. Phys.*, 1994, **100**, 5829–5835.
- 93 M.J. Frisch, G.W. Trucks, H.B. Schlegel, G.E. Scuseria, M.A. Robb, J.R. Cheeseman, G. Scalmani, V. Barone, B. Mennucci, G.A. Petersson, H. Nakatsuji, M. Caricato, X. Li, H.P. Hratchian, A.F. Izmaylov, J. Bloino, G. Zheng, J.L. Sonnenberg, M. Hada, M. Ehara, K. Toyota, R. Fukuda, J. Hasegawa, M. Ishida, T. Nakajima, Y. Honda, O. Kitao, H. Nakai, T. Vreven, J.A. Montgomery, Jr., J.E. Peralta, F. Ogliaro, M. Bearpark, J.J. Heyd, E. Brothers, K.N. Kudin, V.N. Staroverov, T. Keith, R. Kobayashi, J. Normand, K. Raghavachari, A. Rendell, J.C. Burant, S.S. Iyengar, J. Tomasi, M. Cossi, N. Rega, J.M. Millam, M. Klene, J. E. Knox, J.B. Cross, V. Bakken, C. Adamo, J. Jaramillo, R. Gomperts, R.E. Stratmann, O. Yazyev, A.J. Austin, R. Cammi, C. Pomelli, J.W. Ochterski, R.L. Martin, K. Morokuma, V.G. Zakrzewski, G.A. Voth, P. Salvador, J.J. Dannenberg, S. Dapprich, A.D. Daniels, O. Farkas, J.B. Foresman, J.V. Ortiz, J. Cioslowski, and D.J. Fox, Gaussian 09 (Revision D.01) Gaussian Inc., Wallingford CT, 2013.
- 94 R. Dennington, T. Keith and J. Millam, GaussView, version 5, Semichem Inc., Shawnee Mission, KS, 2009.
- 95 D.G. Wei, W.D. Wilson and S. Neidle, *J. Am. Chem. Soc.*, 2013, **135**, 1369–1377.
- 96 W. Zhu, Y. Wang, K. Li, J. Gao, C.H. Huang, C.C. Chen, T.P. Ko, Y. Zhang, R.T. Guo and E. Oldfield, *J. Med. Chem.*, 2015, **58**, 1215–1227.
- 97 S. Curry, H. Mandelkow, P. Brick and N. Franks, *Nat. Struct. Biol.*, 1998, **5**, 827–835.
- 98 J. Ghuman, P.A. Zunszain, I. Petitpas, A.A. Bhattacharya, M. Otagiri and S. Curry, *J. Mol. Biol.*, 2005, **353**, 38–52.
- 99 Z.M. Wang, J.X. Ho, J.R. Ruble, J. Rose, F. Ruker, M. Ellenburg, R. Murphy, J. Click, E. Soistman, L. Wilkerson and D.C. Carter, *Biochim. Biophys. Acta*, 2013, **1830**, 5356–5374.
- 100 M. F. Sanner, *J. Mol. Graphics Modell.*, 1999, **17**, 57–61.
- 101 G.M. Morris, R. Huey, W. Lindstrom, M.F. Sanner, R.K. Belew, D.S. Goodsell and A.J. Olson, *J. Comput. Chem.*, 2009, **16**, 2785–2791.
- 102 O. Trott and A.J. Olson, *J. Comput. Chem.*, 2010, **31**, 455–461.
- 103 E.F. Pettersen, T.D. Goddard, C.C. Huang, G.S. Couch, D.M. Greenblatt, E.C. Meng and T.E. Ferrin, *J. Comput. Chem.*, 2004, **25**, 1605–1612.